UNIVERSIDADE FEDERAL DO RIO GRANDE DO SUL

INSTITUTO DE FÍSICA

Development of an ultrasensitive technique for optical characterization measurements[1]

Érico Motter Braun

Dissertation conducted under the supervision of Professor Dr. Ricardo Rego Bordalo Correia and presented to the Institute of Physics of UFRGS in partial fulfillment of the requirements to obtain the title of Master in Physics.

Porto Alegre
June 2022.

---

[1] This study was financed by the Conselho Nacional de Desenvolvimento Científico e Tecnológico (CNPq).

Agradecimentos

Ao longo deste trabalho várias pessoas foram importantes a mim, e portanto gostaria de agradecê-las:

- Começando pelo meu orientador, Prof. Ricardo, por toda sua dedicação e por toda sua confiança durante sua orientação. Foram muitas as discussões, tanto por chamadas de Zoom quanto no laboratório, e todas foram muito valiosas ao meu aprendizado ao longo desses dois anos.
- Aos meus pais, Thomas e Luci, e à minha irmã, Anelise, que passaram a maioria do tempo juntos comigo nesse tempo de pandemia. Sou muito grato a todo o apoio e amor que depositaram em mim desde antes deste trabalho.
- Ao Prof. Ismael, que revisou o inglês deste trabalho e ajudou a elucidar muitas passagens do texto.
- Aos meus colegas, Amanda e Vinícius, por compartilhar suas experiências e tornar o dia-a-dia no laboratório mais divertido.
- Aos meus amigos Pedro e Ana, que alegram muitas das noites e finais de semana desses últimos anos. Também agradeço a todo pessoal do RPG, por tornar as quartas-feiras em um dos melhores dias da semana.
- Por fim, agradeço ao CNPq, sem seu apoio financeiro não seria possível realizar este trabalho.

Abstract

We review the mathematical structure used in quantum mechanics (namely vector spaces) to show how the property of non-separability arises. In this context, non-separability is called quantum entanglement, and we explore some of its history and the consequences of this concept. Based on a mathematical discussion, we also explore non-separability in the context of classical optics, which recently sparked interest due to the finding that entanglement-like correlations can arise even with classical fields. Weak measurements are then introduced as an application of non-separability, where the entanglement created by a weak interaction is manipulated to amplify the measured value. Finally, we propose an experimental implementation of a weak valued beam deflection measurement, capable of measuring small values of the nonlinear refractive index through the weak valued amplification. In addition to this latter amplification, we also found a dependence of our signal with the beam's waist, which for a Gaussian beam is tantamount to an amplification with the propagation distance.

Resumo

Revisamos a estrutura matemática utilizada na mecânica quântica (principalmente espaços vetoriais) para mostrar como a propriedade de não-separabilidade emerge. Neste contexto, não-separabilidade é chamada de emaranhamento quântico, e exploramos um pouco de sua história e as consequências desse conceito. Baseando-se na discussão matemática, também exploramos não-separabilidade no contexto de óptica clássica, o que recentemente despertou interesse pelo achado que correlações similares às do emaranhamento podem ocorrer mesmo com campos clássicos. Medidas fracas são então introduzidas como uma aplicação de não-separabilidade, onde o emaranhamento criado por uma interação fraca é manipulada para amplificar o valor medido. Enfim, propomos uma implementação experimental de uma medida de desvio de feixe utilizando valores fracos, capaz de medir pequenos valores do índice de refração não-linear através da amplificação de valores fracos. Além desta amplificação, encontramos uma dependência do sinal com a cintura do feixe, o que é equivalente a uma amplificação dependente da distância de propagação para feixes gaussianos.

Index

Introduction **6**

1 Entanglement **8**
- 1.1 Vector spaces 8
  - 1.1.1 Tensor product spaces 11
- 1.2 Quantum mechanics and entanglement 12
  - 1.2.1 Applications of quantum entanglement 13
- 1.3 Classical electromagnetism and ‘entanglement’ 16
  - 1.3.1 Applications of classical non-separability 18

2 Weak values **23**
- 2.1 Von Neumann-type measurements 23
- 2.2 Weak measurements 26
- 2.3 Applications of weak measurements 29

3 Nonlinear optical effects **31**
- 3.1 Linear optics 31
  - 3.1.1 Gaussian beams 31
  - 3.1.2 Linear polarization 34
- 3.2 Nonlinear polarization 35
  - 3.2.1 Third order effects 36
  - 3.2.2 Beam deflection technique 38

4 Amplification of third order optical effects with weak measurements **41**
- 4.1 Experimental setup 41
- 4.2 Results 48
  - 4.2.1 OG515 48
  - 4.2.2 Acetone 51

Concluding remarks **53**

A Fisher information and the Cramér-Rao bound **55**
- A.1 Fisher information 55
- A.2 Cramér-Rao bound 56

References **63**

Introduction

In the first decades of the 20th century, quantum mechanics revolutionized the way physicists described and interacted with the microscopic world. This novel description of physical reality, through a probabilistic wave-like behavior, introduced many concepts seemingly at odds with the old and successful descriptions of the now named classical world. In particular, the non-local probabilistic measurement interpretation and the possibility that parts of a system might be influenced over large distances were a topic of heated debate since their introduction in the seminal works of Schrödinger, Bohr, Heisenberg and others. This influence over large distances, which received the name of "entanglement", is perhaps most widely known from the debates between Einstein and Bohr, since paradoxes and other inconsistencies may arise without a careful interpretation of the theory.

Since the work of Bell in 1964 [9] and from the many experiments made to test it, entanglement was accepted as an inherent feature of physical reality and became a synonymous for quantum-like behavior. The violations predicted by Bell were tested in ever more robust scenarios, and exploitation of the entanglement property allowed for quantum states to be reliably transferred over large distances through the quantum teleportation protocol. However, in recent years more careful observations found that correlations similar to those caused by entanglement can be achieved by purely classical means. Even without the non-local aspect of measurements, classical optics can support effects such as Bell-like inequalities violations and state teleportation (which works similarly to quantum teleportation).

This "classical entanglement", or more appropriately called "classical non-separability", is possible due to the very similar mathematical structure shared between quantum mechanics and classical optics. Both of these theories are built from the mathematical concept of vector spaces, and the non-separability naturally arises when vector spaces are combined to create a tensor product space. As such, we dedicate part of Chapter 1 to review vector spaces and introduce the tensor product operation, and later we explore quantum entanglement and its consequences. Finally, classical non-separability is explored as a parallel to quantum entanglement, outlining the similarities and differences between both.

After the discussion about entanglement, in Chapter 2 we review the metrology technique of weak measurements. A weak measurement is an alternative measurement protocol where a weak interaction entangles two degrees of freedom of a system, and by postselecting the final state a large value can be observed as a result of the interaction. This protocol presents some advantages over the standard non-weak protocol such as an improved signal-to-noise ratio [66] and the possibility to measure ultra-small effects [39, 38], to name a few. Another interesting feature is the possibility to realize weak measurements with classical optics: since they are intrinsically linked to entanglement and interference, they can be analyzed as a special interferometric technique with classical beams. The use of the latter allows for robust tabletop experiments to be made, which can circumvent difficulties of manipulating quantum objects in an experimental scenario.

The later half of this work focuses in applying the weak measurement protocol to an already established beam deflection (BD) technique of nonlinear optics. Chapter 3 focuses in reviewing the relevant concepts of nonlinear optics and explaining how the BD technique works, creating a common foundation for the addition of the weak measurement. Then, Chapter 4 describes our implementation and experimental setup, where we investigate the new features the weak measurement introduces to the BD technique.

Chapter 1

Entanglement

Entanglement is at the heart of quantum mechanics, and it is also one of the essential features to perform weak measurements. Although entanglement is commonly discussed as a purely quantum effect, recent research shows an entanglement analogue in classical optics, where no quantum effects occur. For instance, researchers using such "classical entanglement" were even able to violate Bell-like inequalities with purely classical beams [44]. In this chapter, I will show how entanglement (in the more general case called non-separability) is related to the mathematical structure of quantum mechanics and classical optics, namely on their use of vector spaces. I will also show how non-separability arises naturally when we consider tensor products of vector spaces, and how non-separability is to be interpreted in each theory.

1.1 Vector spaces

It is well-known for any physics student that vector spaces play a significant role in many areas of physics: from classical mechanics to the most advanced quantum theories, vector spaces concepts are ingrained in their mathematical foundation. In order to appreciate such a general importance, it's perhaps wise to take a step back and briefly analyze vector spaces from a purely mathematical view, i.e., let's briefly review some concepts from linear algebra. The discussion in this section draws on Cohen-Tannoudji et al. [20], Lang [47] and Sakurai [63].

In mathematics, before we even define a vector space we have to define a *field*. A subset K of the complex numbers $\mathbb{C}$ is said to be a field if the following conditions are satisfied [47]:

1. If x and y are elements of K, then $x + y$ is also an element of K.
2. If x is an element of K, then $-x$ is also an element of K. Also, if $x \neq 0$, x^{-1} is an element of K as well.
3. The elements 0 and 1 are elements of K.

By these conditions, it follows that the complex numbers $\mathbb{C}$ and the real numbers $\mathbb{R}$ (which is a subset of $\mathbb{C}$) are fields. The definition of a field is important because we need a set where addition and multiplication are defined. Finally, some terminology: we call the elements of K simply as *numbers* or *scalars*, when the context in which they appear is clear..

Now, let's define what a vector space is. A vector space V over a field K is a set of objects that obey the following conditions [47]:

1. If u, v are elements of V, then $u + v$ is an element of V.

2. If v is an element of V and c an element of K, cv is an element of V.
3. If u, v, w are elements of V, then
$$(u + v) + w = u + (v + w).$$
4. There's an element of V, denoted by 0, such that for all $u \in V$
$$0 + u = u + 0 = u.$$
5. Given $u \in V$, there exists an element $-u$ such that
$$u + (-u) = 0.$$
6. For all elements $u, v \in V$,
$$u + v = v + u.$$
7. If $c \in K$, then $c(u + v) = cu + cv$.
8. If $a, b \in K$, then $(a + b)u = au + bu$.
9. If $a, b \in K$, then $(ab)u = a(bu)$.
10. For all $u \in V$, we have $1u = u$ (where 1 is the identity in K).

From this set of conditions, it follows that the real numbers are a vector space over themselves, while the complex numbers are a vector space over themselves or over $\mathbb{R}$. It can also be shown that the set of all functions that map elements of a set S into K (i.e., $f : S \longrightarrow K$) is also a vector space over K [47]. For simplicity, we can call the elements of a vector space simply as vectors.

From now on, we will consider the field K to be the complex numbers $\mathbb{C}$, as it is the relevant field in quantum mechanics and in optics. Since we can add vectors together and multiply them by complex numbers, we call a *linear combination* a sum of the form

$$c_1 v_1 + c_2 v_2 + \ldots + c_n v_n,$$

where c_i are complex numbers and v_i are vectors. If all vectors of V can be written as a non-trivial linear combination of v_i, we say that the vectors v_i *span* or *generate* the space V. As such, we may also call the vectors v_i a *basis* of the space V. The choice of basis vectors is not unique, but some basis are more useful than others, as will be discussed next.

A final concept that is also important to remember is the inner product. We denote the inner product of two vectors u, v as the number $\langle u, v\rangle$. The inner product associates vectors to complex numbers and must obey the following properties [47, 63]:

1. $\langle u, v\rangle = \langle v, u\rangle^*$ (where * denotes the complex conjugate).
2. $\langle v, v\rangle \geq 0$, where it is only an equality if v is the 0 vector.
3. If u, v, w are vectors, then $\langle u + v, w\rangle = \langle u, w\rangle + \langle v, w\rangle$.
4. If c is a complex number, then $\langle cu, v\rangle = c^* \langle u, v\rangle$.

These four conditions are sufficient to determine the form of inner product for each vector space. For example, if we are dealing with a space of column vectors of the type

$$u = \begin{bmatrix} u_1 \\ \vdots \\ u_n \end{bmatrix}$$

where u_i are complex numbers, then it is easy to show that inner product $\langle u, v \rangle$ that obeys conditions 1 through 4 is:

$$\langle u, v \rangle = u^\dagger v = \begin{bmatrix} u_1^* & \dots & u_n^* \end{bmatrix} \begin{bmatrix} v_1 \\ \vdots \\ v_n \end{bmatrix} = u_1^* v_1 + \dots + u_n^* v_n, \tag{1.1}$$

where † is the hermitian conjugate, the conjugate transpose of the original matrix.

A vector space equipped with such an inner product that is also a *complete metric space* is called a Hilbert space [47, 32]. From this point on I'll assume we are always working with a Hilbert space.

Another form of the inner product of equal importance is the inner product for a function space. Suppose f and g are continuous functions that map an interval L of the real numbers into the complex numbers ($f, g : L \longrightarrow \mathbb{C}$), i.e., they belong to the vector space of continuous functions defined in L. Then, the appropriate form of the inner product $\langle f, g \rangle$ is:

$$\langle f, g \rangle = \int_L f(x)^* g(x)\, dx. \tag{1.2}$$

The final concept that comes from the definition of inner product is the notion of orthogonality between two vectors: if $\langle u, v \rangle = 0$ and either u or v is not the zero vector, then we say that u is orthogonal to v and vice-versa. And of course, from orthogonality we can define the concept of an *orthogonal basis* for the vector space. A basis v_i of vectors is said to be orthogonal if every basis vector is orthogonal to each other, i.e., if $\langle v_i, v_j \rangle = 0$ if $i \neq j$. By extension, an *orthonormal* basis of vectors e_i satisfies

$$\langle e_i, e_j \rangle = \delta_{ij}, \tag{1.3}$$

where δ_{ij} is the Kroenecker Delta:

$$\delta_{ij} = \begin{cases} 1, & \text{if } i = j \\ 0, & \text{if } i \neq j \end{cases}$$

The usefulness of the orthonormal basis is immediate since, being a basis, any vector v of the space V can be represented by a linear combination of basis vectors:

$$v = \sum_i c_i\, e_i, \tag{1.4}$$

where c_i are complex numbers. In order to find the specific values of c_i, it is only necessary to take the inner product of v with each basis vector: by equations (1.4) and (1.3)

$$\langle e_i, v \rangle = \sum_j c_j \langle e_i, e_j \rangle = \sum_j c_j \delta_{ij} = c_i.$$

At last, we may also define *operators* as a map from vectors to vectors, and the most important operators in physics are the *linear* operators. An operator A that maps elements from the space V to the space U ($A : V \longrightarrow U$) is linear if

$$A(c_1 v_1 + c_2 v_2) = c_1 A v_1 + c_2 A v_2 \tag{1.5}$$

where $v_1, v_2 \in V$ and c_1, c_2 are complex numbers.

1.1.1 Tensor product spaces

The final vector space to be discussed deserves its own subsection, and it is the *tensor product space*. This is a vector space formed by combining two (or more) vector spaces together through a tensor product, denoted here by $\otimes$. Let's start by the simple case of the tensor product space made from the product of two vector spaces V and W. The tensor product space (or simply the product space), denoted by $V \otimes W$, is the space composed by the elements (called tensors) of the form

$$v \otimes w, \tag{1.6}$$

where $v \in V$ and $w \in W$. The tensor product operation is linear, and as such

$$\begin{aligned}
(v_1 + v_2) \otimes w &= v_1 \otimes w + v_2 \otimes w \\
v \otimes (w_1 + w_2) &= v \otimes w_1 + v \otimes w_2 \\
c(v \otimes w) &= (cv) \otimes w = v \otimes (cw)
\end{aligned}$$

where c is a complex number.

The inner product between two tensors is defined element-wise as

$$\langle v_1 \otimes w_1, v_2 \otimes w_2 \rangle = \langle v_1, v_2 \rangle \langle w_1, w_2 \rangle. \tag{1.7}$$

With the inner product defined for the product space, then we can also extend the notion of an orthogonal basis: if $\{e_i\}$ is a basis of V and $\{f_j\}$ is a basis of W, then a basis of $V \otimes W$ is simply

$$e_i \otimes f_j,$$

and any element t of the space $V \otimes W$ can be represented as a linear combination of the basis vectors of $V \otimes W$

$$t = \sum_{i,j} c_{ij}\, e_i \otimes f_j. \tag{1.8}$$

where $c_{ij} = \langle e_i \otimes f_j, t \rangle$. Again, the choice of basis is not unique.

Just like operators were defined for vector spaces, we may also define operators on tensor product spaces. In this case, if A is a linear operator in the space V and B is a linear operator in W, then a linear operator in the space $V \otimes W$ is

$$A \otimes B. \tag{1.9}$$

Operators written in the form of Eq. (1.9) are to be understood as acting on their own respective spaces:

$$(A \otimes B)(v \otimes w) = (Av) \otimes (Bw).$$

Operators that only act on the vector space V can be written as $A \otimes I_W$, and similarly, $I_V \otimes B$ when the operator only acts on the space W. Here I_V, I_W are the appropriate identity operators in each space.

Due to the tensor product operation, we gain an additional freedom in this space: we can write basis vectors which are not of the separable form (1.6). As an example, consider V to be a two dimensional vector space with an orthonormal basis $\{e_1, e_2\}$, then a basis for the space $V \otimes V$ is

$$e_1 \otimes e_1, \quad e_1 \otimes e_2, \quad e_2 \otimes e_1, \quad e_2 \otimes e_2. \tag{1.10}$$

Another basis for this same space can be made by taking the following linear combinations of elements from (1.10):

$$\begin{aligned} f_1 &= \frac{1}{\sqrt{2}}\left[e_1 \otimes e_1 - e_2 \otimes e_2\right], & f_3 &= \frac{1}{\sqrt{2}}\left[e_1 \otimes e_2 - e_2 \otimes e_1\right], \\ f_2 &= \frac{1}{\sqrt{2}}\left[e_1 \otimes e_1 + e_2 \otimes e_2\right], & f_4 &= \frac{1}{\sqrt{2}}\left[e_1 \otimes e_2 + e_2 \otimes e_1\right]. \end{aligned} \tag{1.11}$$

By taking the inner product between each element of the above, it can be shown that they also form an orthonormal basis for $V \otimes V$. However, this time all the elements f_i of (1.11) can not be written as a tensor product of two vectors of V ($f_i \neq v \otimes w$, for any v, w); they are ‘non-separable’. It is also worth mentioning the non-separable property is more general than the two-dimensional example shown here - any tensor product space supports it. This non-separability is at the core of quantum entanglement, where each basis vector represents a possible quantum state of the system, and having a state in a non-separable form creates a correlation between each of its parts. However, no quantum mechanics was used to derive the non-separable basis (1.11), showing that any theory built with tensor product spaces allows a similar non-separability to be constructed, such as in classical electromagnetism, as will be shown in the next sections. We will now explore the feature of non-separability within the context of quantum mechanics and classical electromagnetism, explaining how this quantum interpretation can be used in the classical theory.

1.2 Quantum mechanics and entanglement

In quantum mechanics, the state of a quantum system is represented by a state vector $|\psi\rangle$ in a Hilbert space $\mathcal{H}$, with the restrictions that it must be normalized ($\langle\psi|\psi\rangle = 1$) and solves the Schrödinger equation:

$$\hat{H}|\psi\rangle = i\hbar\frac{\partial}{\partial t}|\psi\rangle, \tag{1.12}$$

where $\hat{H}$ is the hamiltonian operator, representing the total energy of the system [20, 63]. This arbitrary quantum state can be expanded by defining a basis in its Hilbert space $\mathcal{H}$. Typically, this basis is formed by the eigenstates of an hermitian operator[1] $\hat{A}$ that commutes with the hamiltonian ($[\hat{H}, \hat{A}] = \hat{H}\hat{A} - \hat{A}\hat{H} = 0$), with the interpretation that whenever this condition is satisfied both observables corresponding to $\hat{H}$ and $\hat{A}$ can be observed simultaneously, classifying them as *compatible observables* [20, 63]. As an example relevant to this work, we may take $\mathcal{H}$ to be a two-dimensional Hilbert space, with the basis vectors $|0\rangle$ and $|1\rangle$ being eigenstates of the operator $\hat{A}$ with

$$\begin{aligned} &|0\rangle \text{ with eigenvalue } 0, \\ &|1\rangle \text{ with eigenvalue } 1. \end{aligned}$$

Due to $|0\rangle, |1\rangle$ being eigenvectors of an hermitian operator, it can be shown that they are already orthogonal to each other [20, 63], thus we may take them to be orthonormal as well.

---

[1] An operator is considered hermitian if $\hat{A}^\dagger = \hat{A}$, where † is the hermitian conjugate.

The two-dimensional Hilbert space $\mathcal{H}$ is a general example of a single particle space, in this case also called a *qubit* as it represents the simplest form of a quantum bit of information. Now, if the system is composed of two qubits A and B, the state vector will now belong to the product space $\mathcal{H}_A \otimes \mathcal{H}_B$, whose basis will be similar in structure to (1.10):

$$|0\rangle_A|0\rangle_B, \quad |0\rangle_A|1\rangle_B, \quad |1\rangle_A|0\rangle_B, \quad |1\rangle_A|1\rangle_B, \tag{1.13}$$

where the subscripts A and B refer to which qubit the individual state vector belongs to[2]. From the basis (1.13), we can create an *entangled* basis for the state vectors of this system as [37]

$$\begin{aligned} |\phi^\pm\rangle &= \frac{1}{\sqrt{2}}\big(|0\rangle_A|0\rangle_B \pm |1\rangle_A|1\rangle_B\big), \\ |\psi^\pm\rangle &= \frac{1}{\sqrt{2}}\big(|0\rangle_A|1\rangle_B \pm |1\rangle_A|0\rangle_B\big). \end{aligned} \tag{1.14}$$

These states are also called the *maximally entangled states* or *Bell states* [37], the reason for the latter is due to their relationship with the Bell inequalities.

The state vectors of (1.14) are entangled since they cannot be written as a product of individual state vectors of A and B:

$$|\psi^\pm\rangle \neq |\psi\rangle_A|\phi\rangle_B \tag{1.15}$$

for any choice of one qubit state vectors $|\psi\rangle_A$ and $|\phi\rangle_B$. The same applies for the states $|\phi^\pm\rangle$.

Due to the postulates of quantum mechanics, a measurement on a quantum system will collapse its state vector onto one of the eigenvectors of the measured observable. Thus, the implications of the entangled state vectors (1.14) are apparent: if a measurement is made on a single qubit of an entangled state it has equal probability of being found in either state 0 or 1, thus we have no knowledge of each individual qubit that makes up the system [37]. However, once a measurement is made on a qubit, we know for *certain* the state of the other qubit. This high correlation between the two constituent qubits is a key feature of entanglement, and has found wide use since its discovery, from a deep insight into the theoretical framework of quantum mechanics to real world applications of quantum protocols [37]. In what follows I'll briefly discuss some of the applications of quantum entanglement.

1.2.1 Applications of quantum entanglement

One of the earliest discussions and perhaps the most famous that features entangled states is the EPR paradox. In 1935, Einstein, Podolsky and Rosen proposed a thought experiment where they considered correlations between position and momentum measurements on a pair of entangled particles separated by an arbitrary distance [26]. Based on the postulates of quantum mechanics, they argued that the theory would violate no faster than light communication or would be incomplete to describe physical reality [26, 62]. Another formulation of the thought experiment attributed to Bohm analyzes spin rather than position-momentum measurements [13, 62], and this is the formulation that common quantum mechanics textbooks, like Griffiths [32] and Sakurai [63] follow.

Consider two observers, Alice and Bob, separated by an arbitrary distance. Midway through, a source prepares two electrons on the singlet state

$$|\psi^-\rangle = \frac{1}{\sqrt{2}}\big(|+z\rangle|-z\rangle - |-z\rangle|+z\rangle\big)_{AB} \tag{1.16}$$

---

[2] In the bra-ket notation of quantum mechanics is customary to drop the tensor product symbol "⊗" between kets.

where $|\pm z\rangle$ are eigenvectors of the Pauli matrix σ_z (i.e., $\sigma_z|\pm z\rangle = \pm|\pm z\rangle$). Since spin 1/2 can only take values of +1 or −1, this system is isomorphic to (1.14). After preparing the singlet state, the source shoots one electron to Alice and the other to Bob. If Alice makes a measurement of σ_z (the spin in the z-direction) on her particle, she will find with equal probability the result +1 or −1. If she measures say, +1, Bob's measurement must necessarily be −1, since by (1.16) their measurements will be anti-correlated. If Bob instead decides to measure the spin on the x-direction, represented by the Pauli matrix σ_x with eigenvectors [20, 63]

$$|\pm x\rangle = \frac{1}{\sqrt{2}}\big(|+z\rangle \pm |-z\rangle\big) \tag{1.17}$$

and thus, after Alice's $+z$ measurement, the state of the system will be

$$|+z\rangle_A|-z\rangle_B = \frac{1}{\sqrt{2}}|+z\rangle_A\big(|+x\rangle - |-x\rangle\big)_B \tag{1.18}$$

and thus Bob will measure with equal probability +1 or −1, making his measurements completely uncorrelated to Alice's. This is no surprise, since σ_z and σ_x do not commute and thus are incompatible observables [20, 32, 63]. But if instead of measuring σ_z, Alice decides to measure σ_x as well, we can rewrite (1.16) to the x-direction basis as [63]

$$|\psi^-\rangle = \frac{1}{\sqrt{2}}\big(|-x\rangle|+x\rangle - |+x\rangle|-x\rangle\big)_{AB} \tag{1.19}$$

and the anti-correlation of Alice's and Bob's measurements return. In their paper, Einstein, Podolsky and Rosen concluded that in order for such correlations to occur the results of each measurement would have to be predetermined in order to not violate Einstein's locality principle (which says that spatially separated parts of a system should be independent from each other). But that would require a hidden variable responsible for such predetermined outcomes, which would imply that quantum mechanics is an incomplete description of reality [26, 62].

The first part of the solution of this Paradox is to show that indeed quantum mechanics is non-local (i.e., it violates Einstein locality principle), but it does not violate causality [63]. In order to prove this, we have to consider a string of measurements on σ_z made by Alice and Bob. Each of their measurements are perfectly anti-correlated, but it is impossible for them to infer that based on their measurements *only*. They would have to compare their strings of measurements using a conventional slower than light way, and thus no new information was transferred before the comparison, preserving causality [62, 63]. Even if Alice and Bob both agree beforehand to measure σ_z, but then Alice suddenly changes to σ_x midway through the experiment, it is impossible for Bob to know that [63]. All that Bob will measure will be a string of randoms +1 and −1s, and will only notice the lack of correlation between the measurements *after* they compare their results, transferring no new information again [63].

It is remarkable that a thought experiment based on a single entangled state led to a deeper insight of quantum theory, namely that it is non-local. The second conclusion of the EPR paradox, however, had to wait until 1964 for Bell to rule out the possibility of a local hidden-variable theory [32, 62]. In short, Bell showed that a local hidden-variable theory would have to obey a specific inequality, while quantum mechanics predicts incompatible results with such inequality [37, 62].

In his original paper [9], Bell considered a general local hidden-variable theory and arrived at an inequality involving the expectation value of the product of the observables A, A', measured by Alice, and B, B', measured by Bob, assuming Alice's and Bob's measured outcomes are perfectly anti-correlated. Typically, the four observables A, A', B, B' are taken to be the spin observables, and can be rotated by an arbitrary angle in relation to each other [37]. A more general inequality without the assumption of anti-correlation was derived by Clauser et al. in 1969 [19], and is known as the Bell-CHSH inequality [37, 62]. They arrived at the general expression

$$S = E(A,B) - E(A,B') + E(A',B) + E(A',B'), \tag{1.20}$$

where $E(X,Y)$ is the expectation value of the product XY. For a local hidden-variable theory, they showed that S is bounded by [19, 37]

$$|S| \leq 2. \tag{1.21}$$

In the quantum case, some configurations can violate this bound (for instance, any of the maximally entangled states (1.14)), in fact, quantum mechanics can achieve the maximum value of [19, 32, 37]

$$|S_{\text{quantum}}| = 2\sqrt{2}. \tag{1.22}$$

This violation of the inequality (1.21) was a firm proof that any local hidden variable theory cannot reproduce the results from quantum mechanics [9, 19, 37]. Since then, the higher than usual correlation arising from entanglement was used as one of the definite signs of quantum behavior [58].

The experimental realizations of the EPR paradox and Bell inequality violations started in the 1970s, however only in the early 1980s it was possible to achieve an unambiguous violation by tens of standard deviations using photon pairs from atomic cascades due to advancements in laser physics [6]. In the late 1980s was already possible to realize EPR-type experiments on the continuous degrees of freedom (as originally proposed by Einstein) on photon pairs coming from spontaneous parametric-down conversion, once again confirming the results from Bell [6].

Another interesting feature of quantum entanglement is the possibility for a qubit to be transferred between Alice and Bob through a maximally entangled state, which is known as *quantum teleportation*. The teleportation protocol goes as follows [10, 37]: Alice has at her site the following qubit

$$|q\rangle_C = \alpha|0\rangle_C + \beta|1\rangle_C \tag{1.23}$$

and wants to transfer it to Bob, which is spatially separated from Alice. Beforehand, they agree on sharing a maximally entangled state (1.14), in this case the $|\phi^+\rangle$ one. Therefore, the state of the entire quantum system is

$$|\psi_{ABC}\rangle = \frac{1}{\sqrt{2}}\big(|0\rangle|0\rangle + |1\rangle|1\rangle\big)_{AB} \otimes |q\rangle_C. \tag{1.24}$$

Alice then makes a projective measurement on her side of the system, but the basis chosen to project is the entangled basis between the qubits A and C. Eq. (1.24) can be written in this entangled basis in the following way [37]

$$\begin{aligned} |\psi_{ABC}\rangle =& \frac{1}{2}\big[|\phi^+\rangle_{AC}(\alpha|0\rangle_B + \beta|1\rangle_B) \\ &+ |\phi^-\rangle_{AC}(\alpha|0\rangle_B - \beta|1\rangle_B) \\ &+ |\psi^+\rangle_{AC}(\alpha|1\rangle_B + \beta|0\rangle_B) \\ &+ |\psi^-\rangle_{AC}(\alpha|1\rangle_B - \beta|0\rangle_B)\big]. \end{aligned} \tag{1.25}$$

When Alice projects the system onto the AC basis, Bob's qubit shares a similar structure to the initial qubit $|q\rangle_C$, albeit it is not necessarily equal to it. In order to make Bob's state be the same as $|q\rangle_C$, Alice shares with Bob the result of her measurement on AC through a classical communication channel. Depending on which state she got, Bob makes the appropriate rotation on his state (realized through the Pauli matrices) to get the desired state, successfully teleporting the state $|q\rangle_C$ to Bob's site.

Quantum teleportation was first proposed in theory by Bennett et al in 1993, and ever since it has been an essential tool in many quantum communication protocols [37]. On the experimental side, the first realization of teleportation was reported in 1998 by Boschi et al [15] with entangled photons over a distance of 2.5 m. This distance has increased over time, culminating in a successful teleportation over 143 km reported by Ma et al in 2012 [51].

Most experimental realizations of quantum entanglement use photon pairs coming from spontaneous parametric down-conversion (SPDC), where an incoming pump photon with frequency ω_0 is split by a nonlinear crystal into two photons of frequencies ω_1 and ω_2, conserving energy in the process: $\omega_1 + \omega_2 = \omega_0$ [49]. Depending on the configuration, this photon pair is entangled and has a high degree of spatial correlation [49]. The caveat of this method is the low efficiency of conversion: usually less than 4 pairs are created for every 10^6 pump photons [12]. There's also the problem of keeping the entanglement of the pair: environment perturbations can cause the entanglement to be lost, which makes keeping the entangled pair a very delicate task [58].

1.3 Classical electromagnetism and 'entanglement'

Although entanglement is typically thought as an exclusively quantum feature, classical electromagnetism allows for a similar non-separability between the degrees of freedom of the electromagnetic (EM) field. In order to appreciate this non-separability, let's start from the basics. The EM field is described by the Maxwell Equations, which for the free fields (far from sources) and in SI units read [42, 31]

$$\nabla \cdot \mathbf{E} = 0 \tag{1.26}$$

$$\nabla \cdot \mathbf{B} = 0 \tag{1.27}$$

$$\nabla \times \mathbf{E} = -\frac{\partial \mathbf{B}}{\partial t} \tag{1.28}$$

$$\nabla \times \mathbf{B} = \mu_0 \epsilon_0 \frac{\partial \mathbf{E}}{\partial t}. \tag{1.29}$$

As it is well-known, these equations describe EM waves for the fields **E** and **B**. By taking the curl of Eq. (1.28) and using Eq. (1.29),

$$\nabla \times (\nabla \times \mathbf{E}) = -\frac{\partial}{\partial t}(\nabla \times \mathbf{B}) = -\mu_0 \epsilon_0 \frac{\partial^2 \mathbf{E}}{\partial t^2}. \tag{1.30}$$

Using the following vector calculus identity

$$\nabla \times (\nabla \times \mathbf{F}) = \nabla(\nabla \cdot \mathbf{F}) - \nabla^2 \mathbf{F} \tag{1.31}$$

and Eq. (1.26), the right hand side of Eq. (1.30) becomes

$$\nabla \times (\nabla \times \mathbf{E}) = -\nabla^2 \mathbf{E}. \tag{1.32}$$

Thus, the electric field **E** obeys the wave equation

$$\nabla^2 \mathbf{E} - \frac{1}{c^2} \frac{\partial^2 \mathbf{E}}{\partial t^2} = 0 \tag{1.33}$$

where $c = 1/\sqrt{\mu_0\epsilon_0}$ is the speed of light in vacuum. A similar procedure yields the wave equation for the magnetic field **B**:

$$\nabla^2\mathbf{B} - \frac{1}{c^2}\frac{\partial^2\mathbf{B}}{\partial t^2} = 0. \tag{1.34}$$

Eqs. (1.33) and (1.34) are not independent from each other however, the electric and magnetic fields are constrained by the Maxwell Equations (1.28) and (1.29). We can then choose any of the wave equations to be our starting point, and the other field can be found by invoking this constraint. Usually in optics the wave equation for the electric field (1.33) is the one chosen. Then, since electromagnetism describes vector fields (in the Euclidean 3-dimensional sense), we can seek solutions to Eq. (1.33) of the form

$$\mathbf{E} = \mathbf{e}_x\, E_x(\mathbf{r}, t) + \mathbf{e}_y\, E_y(\mathbf{r}, t) \tag{1.35}$$

where $\mathbf{e}_x$, $\mathbf{e}_y$ are orthonormal vectors and $E_i(\mathbf{r}, t)$ is a function that solves the *scalar* wave equation:

$$\left(\nabla^2 - \frac{1}{c^2}\frac{\partial^2}{\partial t^2}\right) E_i(\mathbf{r}, t) = 0 \tag{1.36}$$

In this context, $\mathbf{e}_i$ represents the polarization of the electromagnetic wave and $E_i(\mathbf{r}, t)$ its amplitude.

Although this fact is somewhat overlooked, Eq. (1.35) already shows a form of polarization-amplitude "entanglement" [58]. Just by its mathematical structure, it neatly ties back with the discussion about tensor product spaces: as it is well-known from partial differential equations theory, these separable solutions form a basis for the vector space composed of all possible solutions of the wave equation [47]. Therefore, the state of the EM field can be described as a superposition of tensor product elements like Eq. (1.8), allowing for such non-separability between the polarization and the amplitude of the field. If we go even further, we may look for separable solutions of the scalar wave equation (1.36) of the type

$$E_i(\mathbf{r}, t) = F_i(\mathbf{r}) G_i(t) \tag{1.37}$$

which is known as the "separation of variables" procedure. Referring to vector spaces yet again, the functions $F_i(\mathbf{r})$ and $G_i(t)$ are basis functions to their own vector spaces: $F_i(\mathbf{r})$ to the Helmholtz equation and $G_i(t)$ to the harmonic oscillator equation. Since the functions $F_i(\mathbf{r})$ form a basis for their vector space, they are typically chosen to be orthogonal in relation to the inner product (1.2):

$$\int F_i(\mathbf{r}) F_j(\mathbf{r})\, d^3x = 0 \quad \text{if} \quad i \neq j. \tag{1.38}$$

Thus, not only can we interpret the EM field to allow for polarization-amplitude entanglement but we can also realize entanglement between the spatial modes and the temporal modes [58].

As to how to interpret this 'classical entanglement' (more on nomenclature later), consider the following example taken from Qian, Vamivakas and Eberly [58]. We refer back to the separation of variables outlined in Eq. (1.37) but consider now the two distinct superpositions made from the basis functions:

$$E_A(\mathbf{r}, t) = \left[F_1(\mathbf{r}) + F_2(\mathbf{r})\right]\left[G_1(t) + G_2(t)\right] \tag{1.39}$$

$$E_B(\mathbf{r}, t) = F_1(\mathbf{r}) G_1(t) + F_2(\mathbf{r}) G_2(t). \tag{1.40}$$

Eq. (1.39) shows a superposition in each vector space, while (1.40) shows a non-factorizable (or non-separable) superposition of the field. The difference between these two types of superpositions

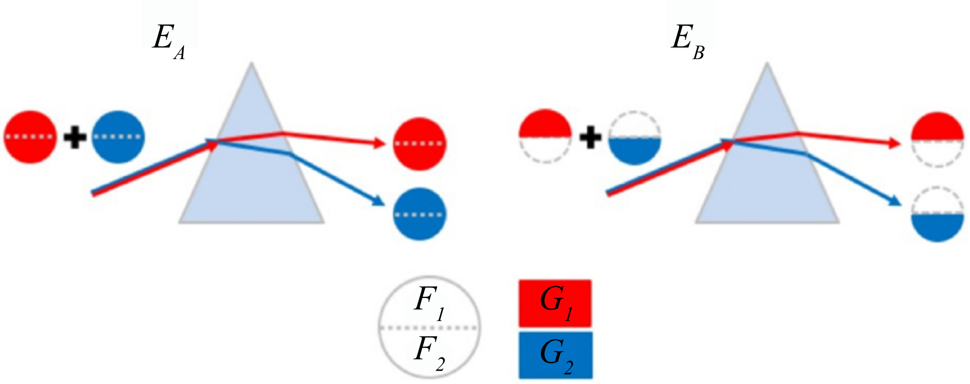

Figure 1.1: example of the distinction between the two superpositions E_A and E_B from Eqs. (1.39) and (1.40), where the F_1, F_2 modes are represented by the upper and lower half circles and G_1, G_2 by the colors red and blue, respectively. Image modified from [58].

of classical fields can be recast in a simple measurement of red and blue frequencies (represented by G_1 and G_2) separated by a prism, as shown in figure 1.1.

Figure 1.1 shows how conditional information is delivered through ‘classical entanglement’: while for the field E_A no information about the spatial modes is acquired after the prism, the E_B field conveys additional information, namely, if the field is present in the upper part or not. This higher than usual correlation between the degrees of freedom is a consequence of the vector space aspect of EM, and doesn’t require any quantum mechanics to be invoked [58].

Speaking of quantum mechanics, now it is a good idea do explain the difference between the ‘true’ quantum entanglement and this ‘classical entanglement’. While a measurement on an entangled quantum system collapses the state onto one of the basis states, the same is not true in the classical case. A measurement of the blue light in figure 1.1 from the field E_B will not change the entire state of the field to blue light only, the red frequency will be still present to be measured after. This is why authors sometimes prefer to use the term ‘classical non-separability’ rather than ‘classical entanglement’, since entanglement is typically associated with the non-local quantum measurement resulting from the wavefunction collapse. Yet, this correlation of classical fields arising from non-separability is of great interest, as will be discussed next.

1.3.1 Applications of classical non-separability

Just like quantum entanglement, classical non-separability allows for a similar correlation between degrees of freedom to be exploited. For instance, one can define classical optical states with a similar structure to quantum states and use them to violate Bell-like inequalities [29, 44]. For the binary degrees of freedom necessary, polarization and path information inside an interferometer can be used through the Jones vector formalism [29]. In this formalism, the polarization of a coherent field of the type

$$\mathbf{E} = (\mathbf{e}_x E_x + \mathbf{e}_y E_y) e^{i(kz-\omega t)} \tag{1.41}$$

is written as the (normalized) Jones vector

$$\mathbf{J} = \frac{1}{\sqrt{(\mathbf{J}\cdot\mathbf{J})}} \begin{bmatrix} E_x \\ E_y \end{bmatrix} \tag{1.42}$$

where $\mathbf{J}\cdot\mathbf{J} = \mathbf{J}^{\dagger}\mathbf{J} = |E_x|^2 + |E_y|^2$ is proportional to the intensity of the field. An example of polarization-path entanglement is a Mach-Zender interferometer as in Fig. 1.2, constructed with two 50:50 beam splitters (BS) and a polarization flipper (PF) in one arm. If a horizontally polarized beam of intensity $I_0 = |E_0|^2$ is incident on the first BS, the polarization degree of freedom will be entangled with the path states **a**, **b**, which effectively act as a two-dimensional orthogonal basis. At the exits of the interferometer the state of the field will be of the form

$$\frac{E_0}{\sqrt{2I_0}}\left[\mathbf{e}_H \otimes \mathbf{a} \pm \mathbf{e}_V \otimes \mathbf{b}\right] \tag{1.43}$$

where $\mathbf{e}_H = [1 \;\; 0]^T$ and $\mathbf{e}_V = [0 \;\; 1]^T$ represent horizontal and vertical polarization, respectively. The path states **a**, **b** can carry information such as phase introduced by placing different optical elements inside the interferometer. The non-separable state (1.43) is also sometimes written in ket form (although no quantum mechanics is involved):

$$\frac{1}{\sqrt{2}}\left[|H\rangle|a\rangle \pm |V\rangle|b\rangle\right]. \tag{1.44}$$

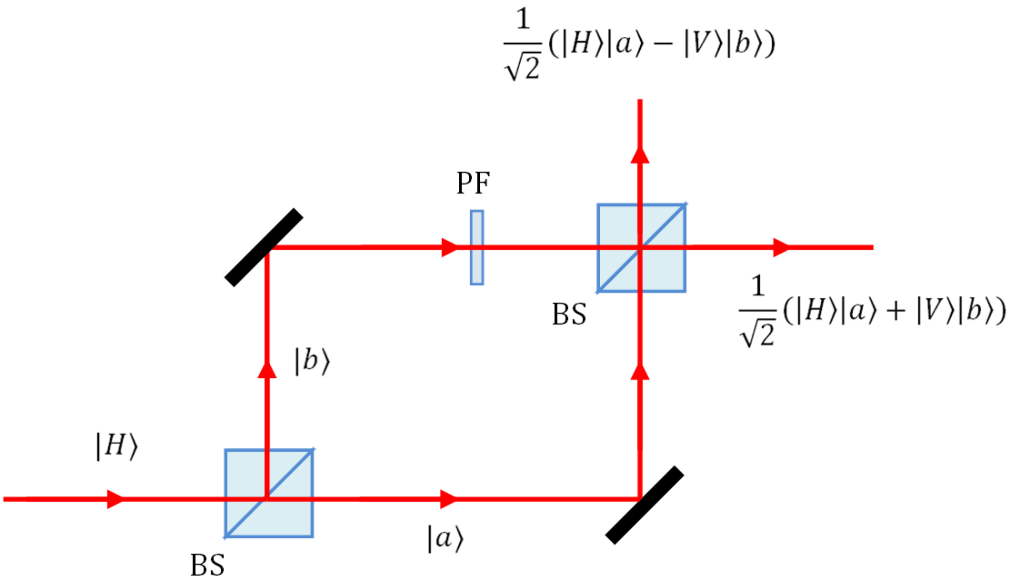

Figure 1.2: a Mach-Zender interferometer can also be thought as a form of entanglement between degrees of freedom of a classical beam. In the figure, a horizontally polarized beam is incident on a 50:50 beam splitter (BS), and on the $|b\rangle$ path the beam has its polarization flipped from $|H\rangle$ to $|V\rangle$ by a polarization flipper (PF). At the exits of the interferometer, the degrees of freedom are correlated and the field is given by Eqs. (1.43) or (1.44).

Just like for the quantum case, one can define correlations between the polarization and path degrees of freedom. For a general separable classical field state of the form

$$\mathbf{E} = \left[\cos\alpha\,\mathbf{e}_H + e^{i\beta}\sin\alpha\,\mathbf{e}_V\right] \otimes \left[\cos\gamma\,\mathbf{a} + e^{i\delta}\sin\gamma\,\mathbf{b}\right], \tag{1.45}$$

the classical equivalent of the S measurement as shown in Eq. (1.20) will also be bounded by $|S_{\text{classical}}| \leq 2$ [29]. However, for the non-separable state (1.44) the $S_{\text{classical}}$ measurement can be greater than 2. In fact, it achieves the same maximum value of $|S_{\text{classical}}| = 2\sqrt{2}$ [29]. These Bell-like violations were experimentally tested using polarization-parity non-separability on coherent and partially coherent beams, with excellent agreement with the theory [44].

Another realization explored the non-separability between the spin (polarization) and orbital angular momentum [14]. Beams with orbital angular momentum are described by the Laguerre-Gaussian modes $\mathrm{LG}_{p,l}$ in cylindrical coordinates [5]. The LG modes can be written as a coherent sum of two Hermite-Gaussian modes $\mathrm{HG}_{n,m}$, which are their cartesian counterpart. For example, the beam $\mathrm{LG}_{0,\pm 1}$ is given by [5]

$$\mathrm{LG}_{0,\pm 1} = \frac{1}{\sqrt{2}}\left[\mathrm{HG}_{1,0} \pm i\,\mathrm{HG}_{0,1}\right]. \tag{1.46}$$

with the HG modes being

$$\mathrm{HG}_{1,0} = E_0\sqrt{\rho}\exp(-\rho/2)\cos\theta \tag{1.47}$$

$$\mathrm{HG}_{0,1} = E_0\sqrt{\rho}\exp(-\rho/2)\sin\theta, \tag{1.48}$$

where $\rho = 2r^2/w^2$ with w being the waist radius of the beam and (r, θ) the polar coordinates.

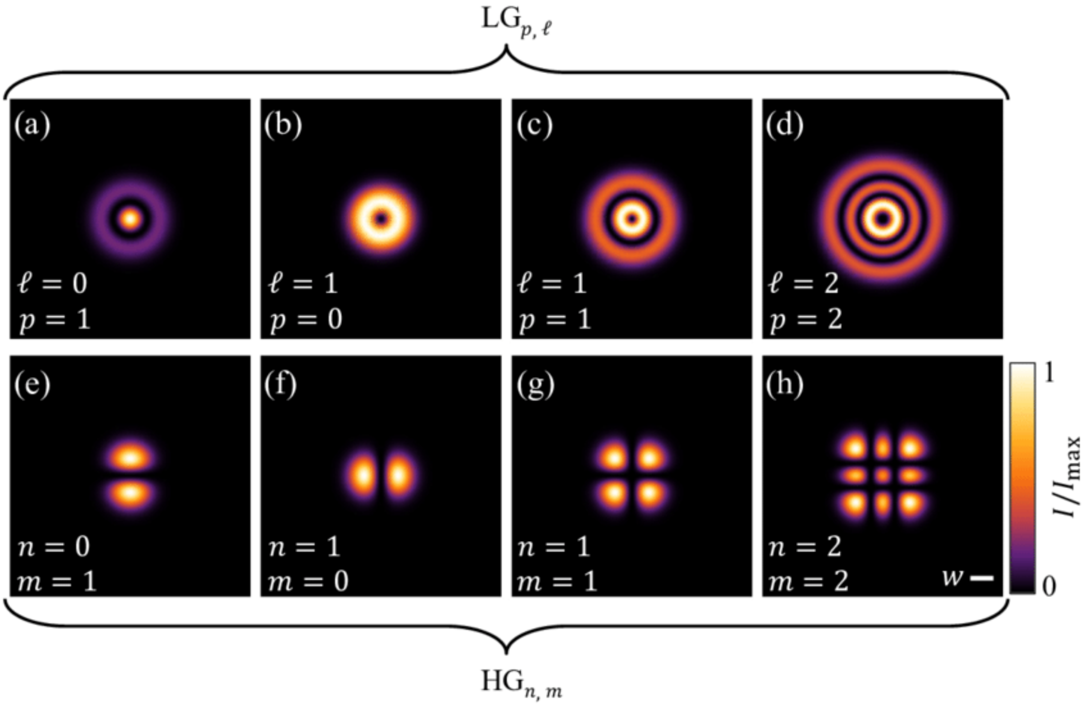

Figure 1.3: some examples of the lowest order Hermite-Gaussian $\mathrm{HG}_{n,m}$ and Laguerre-Gaussian modes $\mathrm{LG}_{p,l}$, taken from [59].

The LG modes with $l \neq 0$ show a typical twist in the phase around the propagation axis (Fig. 1.3), the amount in which the phase twists is associated with the angular momentum of the beam. Due to this twist, the on-axis amplitude must be zero, which gives the LG mode a ring-like shape. While the mode (1.46) is separable, a non-separable spin-orbit mode can be made by considering the following combinations [29]:

$$\mathbf{E}_r = \frac{1}{\sqrt{2}}\left[\mathrm{HG}_{1,0}\,\mathbf{e}_x + \mathrm{HG}_{0,1}\,\mathbf{e}_y\right] = E_0\sqrt{\rho/2}\exp(-\rho/2)\,\mathbf{e}_r \tag{1.49}$$

$$\mathbf{E}_\theta = \frac{1}{\sqrt{2}}\left[\mathrm{HG}_{1,0}\,\mathbf{e}_y - \mathrm{HG}_{0,1}\,\mathbf{e}_x\right] = E_0\sqrt{\rho/2}\exp(-\rho/2)\,\mathbf{e}_\theta \tag{1.50}$$

The result of these non-separable combinations is to create an azimuthally polarized (Eq. (1.50)) and a radially polarized beam (Eq. (1.49)), as can be seen in Fig. 1.4. These non-separable spin-orbit beams were also used on the classical equivalent of quantum teleportation [33]. Hashemi et al [33] developed a protocol to transfer the state from one degree of freedom to another in the same beam. Their experimental realization achieved a 99% fidelity of transfer between the radial modes and polarization [33]. Vortex beams were also used to investigate the interplay between coherence and entanglement in both the classical and quantum domain [57]. It was found that in order to violate intensity based CHSH inequalities the vortex beam must be coherent in both cases, however in the quantum case sub-Poissonian fluctuations in the photon number (below shot-noise) are also required for true entanglement to be realized [57].

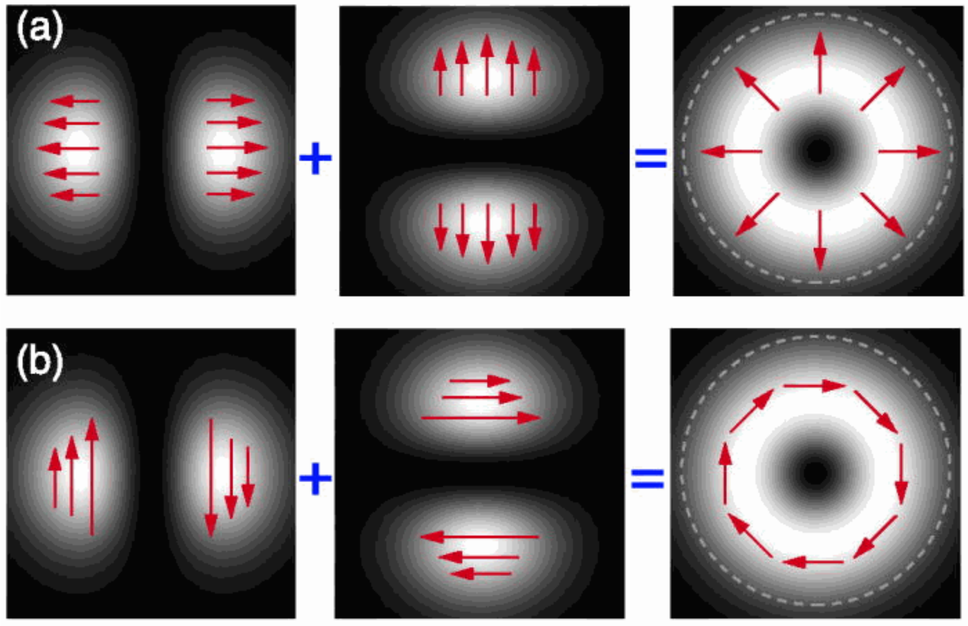

Figure 1.4: intensity (white color) and polarization (red arrows) profiles of the non-separable beams (also known as vector beams), (a) $\mathbf{E}_r$ from Eq. (1.50) and (b) $\mathbf{E}_\theta$ from (1.49). Figure taken from [4].

Just as said in section 1.1, non-separability is a general property of tensor product spaces and is not restricted to two dimensional ones. Indeed, one could realize non-separable combinations between *three* degrees of freedom: path, polarization and transverse mode. A study by Balthazar et al. [7] explored the generation of GHZ-states with classical fields and the violation of the Mermin inequality, which are the equivalents to the Bell-states (1.14) and the Bell-CHSH inequality (1.21) for three degrees of freedom, respectively.

Another revealing application of classical non-separability has been on resolving a longstanding issue in polarization optics [58, 64]. While the two dimensional Jones vectors and 2×2 Jones matrices are sufficient to describe polarization states and linear transformations on fully-polarized coherent beams, one must employ Stokes vectors (which are 4-dimensional) and matrices to describe partially-polarized light [35]. The set of all possible linear transformations one can do on Stokes vectors is known as the Mueller matrices, which is composed of 4×4 matrices that generalize the Jones matrices [35]. However, not every Mueller matrix corresponds to a physical transformation that can be achieved with an optical element [64]. Simon et al [64] showed that in order for a Mueller matrix to be physical its elements must satisfy a stronger positivity criterion, which only follows when linear transformations on non-separable beams are considered.

The advantages of using classical optical beams are apparent: while the generation of an entangled quantum state has often low efficiency and high maintenance, classical beams are easier to generate and are often robust with respect to environment perturbations [58]. Thus they can be used in experiments when the nonlocal character of quantum entanglement is not necessary, exploiting the same correlation that classical non-separability allows between degrees of freedom.

Chapter 2

Weak values

Weak values were first proposed by Aharonov et al in 1988 in their paper titled "How the result of a measurement of a component of the spin of a spin-1/2 particle can turn out to be 100" [2]. And just as the title of the paper highlights, weak values have what is called an anomalous amplification property, where the weak value of an operator can significantly exceed its largest eigenvalue [2]. In this chapter it is explained how the weak value protocol (also called a "weak measurement") introduces the property of anomalous amplification by postselecting the final state of the system. A way to compare weak measurements with conventional measurements is discussed through the Fisher information, which comes from parameter estimation theory.

2.1 Von Neumann-type measurements

By the postulates of quantum mechanics, a measurement of an observable $\hat{A}$ on a quantum system collapses the state of the system onto one of the eigenstates of $\hat{A}$, with a probability equal to the absolute square of the projection of the system's initial state onto the eigenstate [63, 20, 32]. Due to this nature, this type of measurement is usually called a *projective measurement*, since the act of measuring an observable projects the system onto one of its eigenstates. In 1932, Von Neumann described a different measurement protocol, which uses a quantum system with two degrees of freedom to extract information about an unknown parameter [55]. In most practical applications of weak measurements, the degrees of freedom are typically chosen as a discrete and a continuous one [24, 69], and thus I will describe Von Neumann's protocol in this context.

The setup of Von Neumann's protocol is as follows. We start with a quantum system of two degrees of freedom: a qubit (called the "system") and a continuous degree of freedom x or p (called the "meter"), where p is the canonical momentum of x (i.e., the operators satisfy the commutation relation $[\hat{x}, \hat{p}] = i\hbar$). These two degrees of freedom are initially prepared on the separable state:

$$\begin{aligned} |I\rangle &= |i\rangle \otimes \int dx\, \psi(x)|x\rangle \\ &= |i\rangle \otimes \int dp\, \phi(p)|p\rangle \end{aligned} \tag{2.1}$$

where the system's initial state is

$$|i\rangle = c_0|0\rangle + c_1|1\rangle \tag{2.2}$$

with $|0\rangle$ and $|1\rangle$ the eigenstates of an operator $\hat{A}$ (with $|c_0|^2 + |c_1|^2 = 1$) and $\psi(x)$ the position space wavefunction while $\phi(p)$ is the momentum space wavefunction. $\phi(p)$ is related to $\psi(x)$

through a Fourier transform:

$$\phi(p) = \frac{1}{\sqrt{2\pi\hbar}} \int dx\, \psi(x) e^{-ipx/\hbar}. \tag{2.3}$$

Next, we couple the qubit with the meter via an interaction of the type

$$\hat{H}(t) = -g(t)\hat{A} \otimes \hat{x}, \tag{2.4}$$

where $g(t)$ is a function with compact support limiting the duration of the interaction [2]. This leads to a time evolution operator

$$\hat{U} = \exp\left[\frac{ig\hat{A} \otimes \hat{x}}{\hbar}\right], \tag{2.5}$$

where $g = \int_0^T g(t)\, dt$ with T being the interaction time. The parameter g, the interaction strength, is the parameter to be estimated.

The operator (2.5) can be identified as the momentum-space translation operator, but with a momentum shift dependent on the eigenvalues of $\hat{A}$. It is convenient to take $\hat{A}$ as the third Pauli matrix, $\hat{\sigma}_z$, since it will produce equal but opposite momentum shifts of $\pm g$ in momentum space (i.e., the operator will shift the momentum eigenstates $|p\rangle$ to $|p \pm g\rangle$). According to this notation, the eigenstates of $\hat{A}$ are

$$\begin{aligned} \hat{A}|0\rangle &= +|0\rangle \\ \hat{A}|1\rangle &= -|1\rangle, \end{aligned} \tag{2.6}$$

and thus

$$\hat{A} = |0\rangle\langle 0| - |1\rangle\langle 1|. \tag{2.7}$$

The final state $|F\rangle$ of the entire system is given by inserting (2.7) into (2.5) and applying on (2.1):

$$\begin{aligned} |F\rangle &= \hat{U}|I\rangle \\ &= c_0|0\rangle \int dp\, \phi(p)|p+g\rangle + c_1|1\rangle \int dp\, \phi(p)|p-g\rangle \\ &= \int dp\, \left[c_0|0\rangle\, \phi(p-g) + c_1|1\rangle\, \phi(p+g)\right]|p\rangle, \end{aligned} \tag{2.8}$$

As expected by the interaction hamiltonian (2.4), the continuous degree of freedom is now coupled with the qubit degree of freedom. This coupling is also highlighted if we calculate the reduced density matrix over each of the degrees of freedom [53]. The qubit's (system) density matrix is calculated by tracing the global density matrix corresponding to the final state $\hat{\rho} = |F\rangle\langle F|$ over the continuous degree of freedom (meter):

$$\begin{aligned} \hat{\rho}_S = \mathrm{Tr}_M(|F\rangle\langle F|) &= \int dp\, \langle p|F\rangle\langle F|p\rangle \\ &= \begin{pmatrix} |c_0|^2 & c_0 c_1^* \alpha \\ c_0^* c_1 \alpha^* & |c_1|^2 \end{pmatrix} \end{aligned} \tag{2.9}$$

where the subscripts S and M stand for system and meter, respectively. The parameter α, which is a function of g, measures the overlap between the displaced wavefunctions:

$$\alpha(g) = \int dp\, \phi(p+g)\phi^*(p-g). \tag{2.10}$$

In the case of no interaction, $g = 0$, α becomes unity and $\hat{\rho}_S$ describes a pure ensemble, thus we get no information about $\phi(p)$ by measuring the qubit only in this case. However, in the case of a strong interaction, $g^2 \gg \mathrm{Var}[\phi(p)]$[1], α approaches zero and $\hat{\rho}_S$ describes a mixed ensemble. Thus, in the strong interaction regime, we can extract information about the momentum space wavefunction simply by measuring the qubit [53], as was expected from the earlier discussion of entanglement.

In case we want to measure the continuous degree of freedom (the meter), we calculate the meter's reduced density matrix $\hat{\rho}_M$ by taking the trace of $|F\rangle\langle F|$ over the qubit (system) states [53]:

$$\begin{aligned}\hat{\rho}_M &= \mathrm{Tr}_S(|F\rangle\langle F|) = \langle 0|F\rangle\langle F|0\rangle + \langle 1|F\rangle\langle F|1\rangle \\ &= \int dp \int dp' \left[|c_0|^2\phi(p-g)\phi^*(p'-g) + |c_1|^2\phi(p+g)\phi^*(p'+g)\right]|p\rangle\langle p'|. \end{aligned} \tag{2.11}$$

Here we are interested in the expectation value of the momentum p, which is:

$$\begin{aligned}\langle\hat{p}\rangle &= \mathrm{Tr}(\hat{\rho}_M\hat{p}) = \int dp\, pP(p;g) \\ &= \langle\hat{p}\rangle_0 + g\left[|c_0|^2 - |c_1|^2\right] \\ &= \langle\hat{p}\rangle_0 + g\langle i|\hat{A}|i\rangle, \end{aligned} \tag{2.12}$$

where

$$P(p;g) = \langle p|\hat{\rho}_M|p\rangle = |c_0|^2|\phi(p-g)|^2 + |c_1|^2|\phi(p+g)|^2 \tag{2.13}$$

is the probability distribution in momentum space and

$$\langle\hat{p}\rangle_0 = \int dp\, p|\phi(p)|^2 \tag{2.14}$$

is the expectation value of the initial momentum wavefunction. Equation (2.12) shows that the interaction induces a shift on the expectation value of the momentum distribution, but this shift depends on the initial qubit state. In the strong interaction regime, however, even in the case of no shift in $\langle\hat{p}\rangle$ we can still unambiguously associate a measurement of $\hat{p}$ to a specific state $|0\rangle$ or $|1\rangle$, since due to the strong interaction the distribution $P(p;g)$ shows two well-separated peaks, as in figure 2.1.

As a final note, it should be noted that the interaction (2.4) does not induce a shift in the position space wavefunction, $\psi(x)$, nor in the probability distribution $P(x;g)$. This can be seen by applying the time evolution operator (2.5) on the position representation:

$$|F\rangle = \hat{U}|I\rangle = \int dx \left[c_0 e^{igx/\hbar}|0\rangle + c_1 e^{-igx/\hbar}|1\rangle\right]\psi(x)|x\rangle. \tag{2.15}$$

The reduced density matrix for the meter in this representation is

$$\hat{\rho}_M = \int dx \int dx' \left[|c_0|^2 e^{ig(x-x')/\hbar} + |c_1|^2 e^{-ig(x-x')/\hbar}\right]\psi(x)\psi(x')|x\rangle\langle x'|, \tag{2.16}$$

and the probability distribution in position space is

$$P(x;g) = \langle x|\hat{\rho}_M|x\rangle = |\psi(x)|^2, \tag{2.17}$$

and thus no shift is induced in this representation.

---

[1] Here Var[ ] stands for the variance measured in the indicated space, i.e.,

$$\mathrm{Var}[\phi(p)] = \langle\hat{p}^2\rangle - \langle\hat{p}\rangle^2 = \int dp\, p^2|\phi(p)|^2 - \left[\int dp\, p|\phi(p)|^2\right]^2.$$

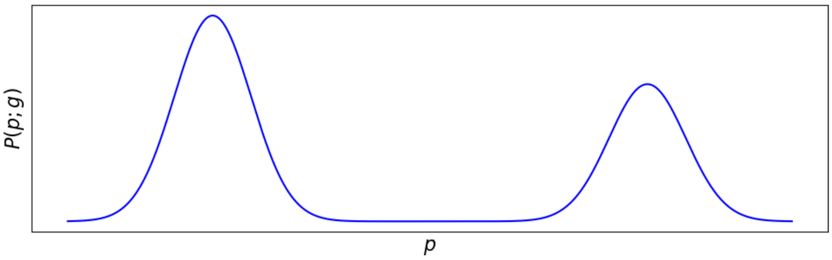

Figure 2.1: Graph of $P(p;g)$ for the meter initially prepared in a gaussian distribution with zero mean $\phi(p) \propto \exp(-p^2/2\Delta^2)$ and with parameters $g = 4\Delta$ (strong interaction), $|c_0|^2 = 0.6$ and $|c_1|^2 = 0.4$. Note that even in the case of $|c_0|^2 = |c_1|^2 = 0.5$ (no shift in $\langle\hat{p}\rangle$), each peak is separated enough to be associated with its respective qubit state.

2.2 Weak measurements

In the last section it was shown how the coupling between the qubit and the position of a particle can be used to measure the interaction strength g. However, the interaction strength can only be measured when it is sufficiently strong to displace each peak in the probability distribution $P(p;g)$. In other words, the measurement protocol described above is restricted to the condition $g^2 \gg \mathrm{Var}[\phi(p)]$. In the opposite limit, $g^2 \ll \mathrm{Var}[\phi(p)]$, Eq. (2.13) shows two highly overlapped peaks, and since g can be considered small, we expand up to first order in g:

$$\begin{aligned} P(p;g) &\approx |c_0|^2 \left(|\phi(p)|^2 - g\frac{d}{dp}|\phi(p)|^2 + \dots\right) + |c_1|^2 \left(|\phi(p)|^2 + g\frac{d}{dp}|\phi(p)|^2 + \dots\right) \\ &\approx |\phi(p)|^2 - \left(|c_0|^2 - |c_1|^2\right) g\frac{d}{dp}|\phi(p)|^2 \\ &\approx |\phi(p - g\langle i|\hat{A}|i\rangle)|^2. \end{aligned} \tag{2.18}$$

Thus, if we want to maximize the estimation of g, we have to maximize the expectation value $\langle i|\hat{A}|i\rangle$. However, the expectation value of any operator is bounded by its maximum eigenvalue [20], which is still a limiting factor in the estimation of small g.

In 1988, Aharonov et al [2] proposed a protocol in this limit of highly overlapped peaks, where they exploited the freedom in the initial and final qubit states. They found that instead of measuring over the initial state $|i\rangle$ like in Eq. (2.11), they could amplify the estimation of g by realizing a post-selection on a final qubit state $|f\rangle$ which is *almost orthogonal* to $|i\rangle$, in the sense that

$$|\langle f|i\rangle|^2 \ll 1. \tag{2.19}$$

Coming back to Eq. (2.5), we use the fact that the interaction strength g is small to expand the time evolution operator up to first order in g:

$$\hat{U} \approx 1 + ig\hat{A} \otimes \hat{x}, \tag{2.20}$$

this approximation is valid whenever $g^2 \ll \mathrm{Var}[\phi(p)]$ [2, 53]. The final global state is therefore

$$|F\rangle = \hat{U}|I\rangle \approx (1 + ig\hat{A} \otimes \hat{x}) \left[|i\rangle \otimes \int dp\, \phi(p)|p\rangle\right]. \tag{2.21}$$

We now perform a post-selection onto a qubit state $|f\rangle$ consistent with the almost orthogonal condition (2.19). Effectively, we are discarding all the measurements that do not project the qubit subsystem onto $|f\rangle$. The state that survives the post-selection is

$$\begin{aligned}(\langle f| \otimes 1)|F\rangle &\approx \langle f|(1 + ig\hat{A} \otimes \hat{x}) \left[|i\rangle \otimes \int dp\, \phi(p)|p\rangle\right] \\ &\approx \langle f|i\rangle \left(1 + ig\langle\hat{A}\rangle_{\mathrm{w}}\, \hat{x}\right) \int dp\, \phi(p)|p\rangle \end{aligned} \tag{2.22}$$

where the weak value of the operator $\hat{A}$ was defined as

$$\langle\hat{A}\rangle_{\mathrm{w}} = \frac{\langle f|\hat{A}|i\rangle}{\langle f|i\rangle}. \tag{2.23}$$

The weak value (2.23) has some interesting properties. Since it is not an expectation value in the usual sense, it is in general a complex number [24]. Furthermore, due to the freedom in selecting the initial and final qubit states, the denominator of (2.23) can be made as small as desired. With a suitable choice of initial and final states, it is possible to make the weak value exceed the biggest eigenvalue of $\hat{A}$ [2, 24]. This last property, usually called ‘anomalous weak value amplification’, is highly valuable in metrology, since it can be used to amplify the estimation of the parameter g to a measurable level [34], as will be shown next.

Since $\langle\hat{A}\rangle_{\mathrm{w}}$ is in general a complex number, let us consider it first as a real one. Then, we can recognize the term inside the parenthesis in Eq. (2.22) as the momentum translation operator for small momentum shifts:

$$1 + ig\langle\hat{A}\rangle_{\mathrm{w}}\, \hat{x} \approx \exp\left(ig\langle\hat{A}\rangle_{\mathrm{w}}\, \hat{x}\right) \tag{2.24}$$

and thus the final probability distribution in momentum space is

$$P_{\mathrm{wv}}(p; g) = |(\langle f| \otimes \langle p|)|F\rangle|^2 \approx |\langle f|i\rangle|^2\, |\phi(p - g\langle\hat{A}\rangle_{\mathrm{w}})|^2. \tag{2.25}$$

Due to the postselection, the momentum translation operator shifts the momentum wavefunction by a value proportional to the weak value of $\hat{A}$.

If the weak value is an imaginary number instead, we change Eq. (2.22) to the position basis and reexponentiate the term inside the parenthesis:

$$(\langle f| \otimes 1)|F\rangle \approx \langle f|i\rangle \int dx\, \psi(x)\, e^{-g\langle\hat{A}\rangle_{\mathrm{w}}\, x}|x\rangle. \tag{2.26}$$

In contrast to the non-postselected measurement, the inclusion of the exponential in Eq. (2.26) induces a shift in the position space wavefunction as well, as can be more easily seen by considering the wavefunction to be a Gaussian, $\psi(x) \propto \exp(-x^2/w^2)$. The probability distribution in position space for this initial Gaussian wavefunction is

$$P_{\mathrm{wv}}(x; g) = |(\langle f| \otimes \langle x|)|F\rangle|^2 \approx |\langle f|i\rangle|^2 \left|\psi(x + g\langle\hat{A}\rangle_{\mathrm{w}} w^2/2)\right|^2. \tag{2.27}$$

Eqs. (2.25) and (2.27) show that we can use both x and p representations to estimate the parameter g. The choice of which to measure is a matter of convenience for the specific experiment to be made. In fact, since imaginary weak values can outperform standard interferometric techniques [17], Eq. (2.27) is the most used for weak valued metrology [53].

Due to weak measurements requiring the postselection onto an almost orthogonal state, it has been objected that this discardment of data outweighs the benefits of the anomalous amplification [53]. In order to show that the discardment of data is not detrimental to weak valued metrology, one must employ a measure through the Fisher information in order to compare weak values to standard techniques. The Fisher information is a statistical concept which measures how much information is available about a parameter g in a random variable X with a probability distribution $P(x;g)$, and it is defined as

$$F(g) = \int \frac{1}{P(x;g)} \left(\frac{\partial P(x;g)}{\partial g} \right)^2 dx \tag{2.28}$$

(see appendix A for a derivation of the Fisher information). It can be shown that for N independent measurements of the random variable X, the Fisher information will be additive: $F_N(g) = NF(g)$. In our case, we are interested in estimating the parameter g from the probability distribution $P(x;g)$. That is why we have to consider an unbiased estimator $\hat{g}$ of the parameter g. Here, "unbiased" means that the expectation value of $\hat{g}$ is equal to g, $\mathrm{E}[\hat{g}] = g$. The importance of this estimator and the Fisher information is due to the following: the variance of the estimator $\hat{g}$ is bounded from below by the Cramér-Rao bound [22]

$$\mathrm{Var}[\hat{g}] \geq \frac{1}{F_N(g)}. \tag{2.29}$$

A derivation of this bound can be found in appendix A. Thus, the Fisher information gives the minimum amount of variance (uncertainty) in our estimation of g. This gives context as to why $F_N(g)$ is called "information": maximization of $F_N(g)$ implies in more quality on the estimation of g. The question left is whether or not a weak valued procedure maximizes the Fisher information in comparison to the standard measurement procedure.

In the conventional Von Neumann measurement for small g, the probability distribution is given by Eq. (2.18). Assuming the momentum space wavefunction is a Gaussian with variance σ^2 and zero mean, $\phi(p) \propto e^{-p^2/4\sigma^2}$, the Fisher information is

$$F_{\text{std}} = N \int \frac{1}{P} \left(\frac{\partial P}{\partial g} \right)^2 dp = \frac{N}{\sigma^2} |\langle i|\hat{A}|i\rangle|^2. \tag{2.30}$$

Since the eigenvalues of the operator $\hat{A}$ are ±1, maximization of the Fisher information happens whenever the initial state $|i\rangle$ is one of the eigenstates, giving a maximal Fisher information of $F_{\text{std}} = N/\sigma^2$. Invoking the Cramér-Rao bound (2.29), the uncertainty $\Delta\hat{g} = \sqrt{\mathrm{Var}[\hat{g}]}$ of our estimator in this case is bounded by

$$\Delta\hat{g} \geq \frac{\sigma}{\sqrt{N}}. \tag{2.31}$$

In the optical case, we interpret N as the average photon number of the EM field since every photon is independent from the other, each representing an independent measurement of the field. For instance, measurements on a coherent EM field are limited by shot noise, which has a variance on the photon number n of $(\Delta n)^2 = N$ [49, 54]. However, the relative uncertainty $(\Delta n)/N = 1/\sqrt{N}$ decreases as the average photon number N increases. Thus the Cramér-Rao bound (2.29) also gives the expected dependency of $1/\sqrt{N}$ for shot noise-limited measurements.

For the weak valued experiment, the probability distribution is given by Eq. (2.25) and the Fisher information is thus

$$F_{\text{wv}} = N \int \frac{1}{P_{\text{wv}}} \left(\frac{\partial P_{\text{wv}}}{\partial g} \right)^2 dp = \frac{N}{\sigma^2} \left|\langle \hat{A} \rangle_{\text{w}}\right|^2 |\langle f|i\rangle|^2. \tag{2.32}$$

With a nonzero $\langle f|i\rangle$, we can use the definition of weak value (2.23) to rewrite (2.32) as

$$F_{\text{wv}} = \frac{N}{\sigma^2} \left|\langle f|\hat{A}|i\rangle\right|^2. \tag{2.33}$$

Maximization of $|\langle f|\hat{A}|i\rangle|^2$ can be more easily understood if we invoke the Bloch sphere for the $|0\rangle, |1\rangle$ states [24]. Since weak values only show anomalous amplification for the case of almost orthogonal initial and final states, we will consider this case. That means that $|f\rangle$ and $|i\rangle$ are almost diametrically apart on the Bloch sphere. Now, the operator $\hat{A} = |0\rangle\langle 0| - |1\rangle\langle 1|$ rotates the state by π radians around the $|0\rangle, |1\rangle$ axis, and thus maximization of $|\langle f|\hat{A}|i\rangle|^2$ only happens when both states $|f\rangle, |i\rangle$ lie close to the equator, since in this configuration the rotated state $\hat{A}|i\rangle$ will be almost equal to $|f\rangle$ (Fig. 2.2). It can never be equal however, because if the initial and final states are orthogonal to each other Eq. (2.25) gives zero probability of postselection and no shift can be observed. Therefore, we conclude that weak measurements *asymptotically* recover all the available Fisher information N/σ^2 as $\langle f|i\rangle \to 0$ [53], showing that the discardment of data does not hinder the anomalous amplification.

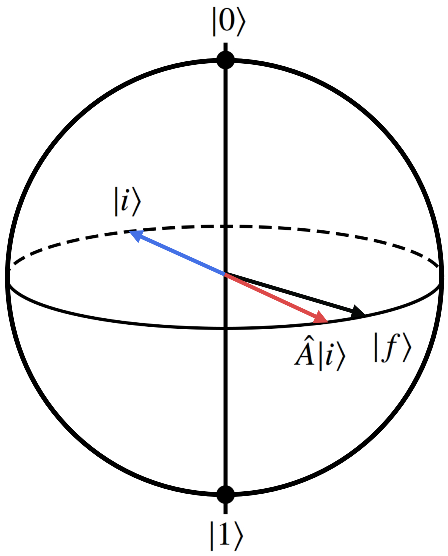

Figure 2.2: Bloch sphere representation of the $|0\rangle, |1\rangle$ states. The initial state $|i\rangle$ (in blue) is almost diametrically opposite to $|f\rangle$ (in black). The rotated state $\hat{A}|i\rangle$ (in red) is almost the same as $|f\rangle$, giving an approximately unity overlap, $\langle f|\hat{A}|i\rangle \approx 1$, and asymptotically maximizing the Fisher information (2.33) as $\langle f|i\rangle \to 0$.

2.3 Applications of weak measurements

The anomalous amplification of weak values can lead to an enhanced signal-to-noise ratio (SNR) in the weak value regime [66] and with imaginary weak values [17] as compared to non-postselected techniques. This SNR enhancement of small signals is sought in gravitational wave detection such as the LIGO (Laser Interferometer Gravitational-Wave Observatory), which had its highest sensitivity located at a narrow band around 100 Hz in its 2016 runs [1]. Due to gravitational wave phenomena ranging from mHz to kHz, it is of great interest to improve the SNR in this broadband range. Based on this problem, weak values are one of the possibilities to enhance low frequency signals [53] while there are already proposals using weak polarization measurements together with squeezed light to improve the SNR in the high frequency regime [40].

In the quantum domain, applications also exist based on the weak values framework. For example, weak measurements can be used to steer quantum systems into pure states, and more recently to mixed states as well [46]. This allows experimental realizations to engineer desired quantum states through variations of the weak measurement's parameters. Weak measurements can also be used as an alternative to quantum tomography, which in some cases can reconstruct the quantum state without the global reconstruction that quantum tomography employs, reducing experimental error propagation in the process [24]. At last, they also found their way into some quantum paradoxes, most notably the "quantum Cheshire cat". In this paradox, the circular polarization of a photon (its spin, an intrinsic property of the particle) can be found in a location where there is no photon at all [3], similar to how the cat in *Alice in Wonderland* can be separated from its grin - hence its name. Instead of solving the paradox, weak measurements further enhance it by making it possible to simultaneously perform both operations of locating the particle and measuring the spin, which in the strong measurement regime wouldn't be possible given that both operations would force the particle state to collapse, thus destroying the paradox [3]. From the weak measurement interpretation, some authors conclude that it is possible to separate an intrinsic property from its particle [3], while others support this is an effect of quantum interference when the quantum states of the detectors are accounted for [21]. Nonetheless, this paradox serves to remind us how important the interpretation of quantum mechanics is when we make conclusions based on it.

Weak values can also be entirely described in terms of classical optics: as outlined in Chapter 1, non-separability is a feature shared by both quantum physics and classical optics. In this classical context, the evolution operator (2.5) is interpreted as a coupling between two degrees of freedom of the same optical beam, for example, its polarization and transverse position. Postselection is achieved by placing polarizers or other optical elements in front of the detector, which results in the same amplification effect of Eqs. (2.25) and (2.27). Many reported weak measurements were made in this classical context, which allowed for robust tabletop experiments such as: measuring the Spin-Hall effect of light [38, 73], ultrasmall beam deflections [23, 36], frequency shifts [67], angular rotations [52] and velocities [41], time delays [17, 68] and temperature changes [25]. Other techniques based on weak values were also used to measure small phases [67, 50] and were even able to achieve anomalous amplification without the need of postselection [54, 48].

Chapter 3

Nonlinear optical effects

In this Chapter we present the basics that constitute the field of nonlinear optics. We begin by describing the basic features of a Gaussian beam, which is the most accurate representation of many experimental laser beams. After briefly reviewing the concept of refractive index from the perspective of the electromagnetic theory, we then move on to the more general case of the nonlinear polarization. We specifically focus on third order effects due to their straightforward inclusion through the nonlinear refractive index, which is the quantity measured in the beam deflection technique.

3.1 Linear optics

3.1.1 Gaussian beams

As seen in Chapter 1, the free Maxwell equations can be simplified to two wave equations for the fields **E** and **B** (whose amplitudes and phases are not independent but instead constrained by the Maxwell equations). As usual in optics, we will work with the electric field, then, it must satisfy

$$\left(\nabla^2 - \frac{1}{c^2}\frac{\partial^2}{\partial t^2}\right)\mathbf{E}(\mathbf{r},t) = 0. \tag{3.1}$$

Let us restrict the solutions of Eq. (3.1) to only electric fields with harmonic time-dependence of the type

$$\mathbf{E}(\mathbf{r},t) = \mathbf{E}(\mathbf{r})e^{-i\omega t}. \tag{3.2}$$

In this case eq. (3.1) becomes the Helmholtz equation for the electric field amplitude $\mathbf{E}(\mathbf{r})$

$$\left(\nabla^2 + k^2\right)\mathbf{E}(\mathbf{r}) = 0. \tag{3.3}$$

where $k^2 = (\omega/c)^2 = (2\pi/\lambda)^2$, where λ is the wavelength.

A basis for the solutions of this equation are the linearly polarized plane waves,

$$\mathbf{e}_i\, e^{i\mathbf{k}\cdot\mathbf{r}} \tag{3.4}$$

where $\mathbf{e}_i$ $(i = 1, 2)$ is a vector perpendicular to $\mathbf{k}$ and $|\mathbf{k}|^2 = k^2 = (\omega/c)^2$. All solutions to Eq. (3.3) can be written as linear combinations of plane waves (3.4).

Despite being able to write any solution of the wave equation as a linear combination of plane waves, in some cases it is more convenient to work with a different basis that better approximates the optical field we are working with. As a relevant case for us, consider laser light: it is highly directional, with minimal divergence and with a finite spatial extent perpendicular to the propagation direction. Plane waves have a definite propagation direction, but they are infinite in extent. This prompts us to seek other solutions of equation (3.1) that better represent these features.

We will restrict ourselves again for the case of linearly polarized waves, and motivated by the plane wave solution (3.4), we will seek solutions to (3.1) that resemble a plane wave modulated by an envelope function, of the form

$$\mathbf{E}(\mathbf{r},t) = \mathbf{E}_0\, u(\mathbf{r}) e^{i(kz-\omega t)}, \tag{3.5}$$

where the propagation direction has been arbitrarily chosen as the z direction. Putting the above ansatz in Eq. (3.1) (where again $\omega^2 = c^2k^2$), we see that the envelope function u must satisfy

$$\nabla_\perp^2 u + \frac{\partial^2 u}{\partial z^2} + 2ik\frac{\partial u}{\partial z} = 0, \tag{3.6}$$

where $\nabla_\perp^2 = \partial^2/\partial x^2 + \partial^2/\partial y^2$ is the transverse laplacian. Now, remember that we are seeking solutions with minimal divergence, which means that the envelope function u must vary slowly with the propagation distance z. This restriction is called the *slowly varying envelope approximation* [16, 71], and in mathematical terms it is written as

$$\left|\frac{\partial^2 u}{\partial z^2}\right| \ll \left|k\frac{\partial u}{\partial z}\right| \tag{3.7}$$

allowing us to neglect the $\partial^2 u/\partial z^2$ term in equation (3.6). In physical terms, it means that many oscillations occur before the envelope substantially changes with the propagation.

With approximation (3.7), u now solves the *paraxial Helmholtz equation*

$$\nabla_\perp^2 u + 2ik\frac{\partial u}{\partial z} = 0. \tag{3.8}$$

The solutions of this equation are the Hermite-Gaussian (HG) modes in cartesian coordinates and Laguerre-Gaussian (LG) modes in cylindrical coordinates [5]. The fundamental solution to both of these families, the $\mathrm{LG}_{0,0} = \mathrm{HG}_{0,0}$ is [71]

$$u(r,z) = \frac{w_0}{w(z)} \exp\left[-\frac{r^2}{w(z)^2}\right] \exp\left[i\frac{kr^2}{2R(z)} - i\psi(z)\right], \tag{3.9}$$

and when inserted back into Eq. (3.5) gives the Gaussian beam solution:

$$\mathbf{E}(\mathbf{r},t) = \mathbf{E}_0\, \frac{w_0}{w(z)} \exp\left[-\frac{r^2}{w(z)^2}\right] \exp\left[ikz + i\frac{kr^2}{2R(z)} - i\psi(z) - i\omega t\right], \tag{3.10}$$

where $r^2 = x^2 + y^2$ and

$$w(z) = w_0\sqrt{1 + \left(\frac{z}{z_R}\right)^2} \text{ is the beam's waist radius,} \tag{3.11}$$

$$z_R = \frac{\pi w_0^2}{\lambda} = \frac{1}{2}k w_0^2 \text{ is the Rayleigh range,} \tag{3.12}$$

$$R(z) = z\left[1 + \left(\frac{z_R}{z}\right)^2\right] \text{ is the radius of curvature,} \tag{3.13}$$

$$\psi(z) = \arctan\left(\frac{z}{z_R}\right) \text{ is the Gouy phase.} \tag{3.14}$$

We see that the Gaussian beam diverges throughout its propagation (figure 3.1), and its waist $w(z)$ takes the minimum value of w_0 at $z = 0$. Also in this region the radius of curvature $R(z)$ becomes infinite, which means the Gaussian beam has no curvature at $z = 0$. Far away from this region ($z \gg z_R$), the waist and the radius of curvature increase linearly.

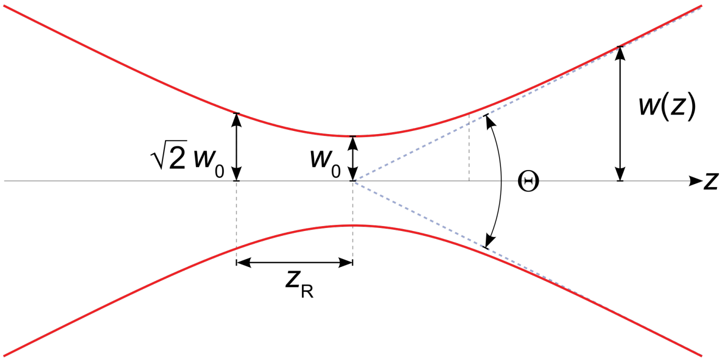

Figure 3.1: schematic featuring the propagation of a Gaussian beam along the z-axis (red line representing the $1/e^2$). The angle Θ is the divergence angle, defined as $\Theta = 2\lim_{z\to\infty} \arctan\big(w(z)/z\big)$. Figure adapted from `https://en.wikipedia.org/wiki/File:GaussianBeamWaist.svg`.

The same propagation effects can be modeled using Fourier optics [30]. Consider the slowly varying amplitude $u(r, z)$ from Eq. (3.9) at $z = 0$, its two-dimensional Fourier transform is

$$\begin{aligned} u(p) &= \frac{1}{2\pi}\int e^{-r^2/w_0^2} e^{-ip_x x - ip_y y}\, d^2x \\ &= \frac{1}{2} w_0^2\, e^{-p^2 w_0^2/4}, \end{aligned} \tag{3.15}$$

where $p^2 = p_x^2 + p_y^2$. In reciprocal space, propagation of the beam by a distance z is equivalent to multiplying $u(p)$ by $\exp(-ip^2 z/2k)$, where $k = 2\pi/\lambda$, and taking an inverse transform [30]:

$$\begin{aligned} u(r, z) &= \frac{1}{2\pi}\int u(p)\exp\left(\frac{-ip^2 z}{2k}\right) e^{ip_x x + ip_y y}\, d^2p \\ &= \left[\frac{w_0^2}{w_0^2 + 2iz/k}\right]\exp\left(-\frac{r^2}{w_0^2 + 2iz/k}\right) \end{aligned} \tag{3.16}$$

This can be simplified by noting that

$$\frac{1}{w_0^2 + 2iz/k} = \frac{1}{w_0^2(1 + iz/z_R)} = \frac{1 - iz/z_R}{w_0^2[1 + (z/z_R)^2]}$$

$$= \frac{1}{w(z)w_0}\exp\big[-i\arctan(z/z_R)\big] \tag{3.17}$$

$$= \frac{1}{w(z)^2} - \frac{ik}{2R(z)}. \tag{3.18}$$

Thus, by substituting the identities (3.17) and (3.18) into (3.16), we recover the result (3.9), showing that indeed this is an equivalent method for propagating Gaussian beams. This method will become advantageous in Chapter 4, where we will analyze the propagation of a Gaussian beam after a small momentum shift is introduced on it.

Finally, the intensity of the optical beam is defined as

$$I(\mathbf{r}) = \epsilon_0 c \langle \mathrm{Re}(\mathbf{E}) \cdot \mathrm{Re}(\mathbf{E}) \rangle_t \tag{3.19}$$

where $\langle\,\rangle_t$ is a time average over the rapid oscillations of the electric field. For fields with a time dependence $e^{-i\omega t}$, it can be shown that (3.19) reduces to

$$I(\mathbf{r}) = \frac{1}{2}\epsilon_0 c |\mathbf{E}(\mathbf{r})|^2. \tag{3.20}$$

Thus, by substituting (3.10) in (3.20), we see that a Gaussian beam also has a gaussian intensity profile:

$$\begin{aligned} I(r,z) &= \frac{1}{2}\epsilon_0 c |\mathbf{E}_0|^2 \left(\frac{w_0}{w(z)}\right)^2 \exp\left(\frac{-2r^2}{w(z)^2}\right) \\ &= I_0 \left(\frac{w_0}{w(z)}\right)^2 \exp\left(\frac{-2r^2}{w(z)^2}\right) \end{aligned} \tag{3.21}$$

where I combined the constants into the peak intensity I_0. Integrating (3.21) over the xy plane gives the total power P carried by the beam:

$$P = \int_{-\infty}^{\infty} dx \int_{-\infty}^{\infty} dy\, I(r,z) = \frac{1}{2}\pi w_0^2 I_0, \tag{3.22}$$

which is independent of z.

3.1.2 Linear polarization

When an electric field $\mathbf{E}$ acts on a neutral, non-magnetic medium, the medium's response is described by its polarization vector $\mathbf{P}$. The polarization is the macroscopic description of the alignment of permanent and induced dipoles to the electric field, and for weak static fields on isotropic media, it is phenomenologically treated as directly proportional to the applied electric field:

$$\mathbf{P} = \epsilon_0 \chi^{(1)} \mathbf{E}. \tag{3.23}$$

Here $\chi^{(1)}$ is known as the linear or first order electrical susceptibility, and assumes different values depending on the medium being described. It's also worth pointing out that for *anisotropic* media $\chi^{(1)}$ becomes a second-rank tensor.

If the incoming electric field is a dynamic quantity, like an electromagnetic wave oscillating with frequency ω, the medium can be dispersive and $\chi^{(1)}$ will be a function of ω, thus (3.23) must be analyzed in frequency domain, where it reads

$$\mathbf{P}(\omega) = \epsilon_0 \chi^{(1)}(\omega) \mathbf{E}(\omega). \tag{3.24}$$

The time-dependent polarization $\mathbf{P}(t)$ is found from (3.24) by taking its Fourier transform and applying the convolution property:

$$\mathbf{P}(t) = \epsilon_0 \int_0^{\infty} R^{(1)}(t') \mathbf{E}(t - t')\, dt', \tag{3.25}$$

where $R^{(1)}(t)$ is known as the linear or first order *response function*, and this convolution between the response function and the electric field states that the polarization at time t depends on the applied electric field at *earlier* times $t - t'$. Here the lower limit $t' = 0$ was explicitly shown, since $R^{(1)}(t') = 0$ for $t' < 0$ in order to not violate causality. The connection between $R^{(1)}(t')$ and $\chi^{(1)}(\omega)$ is also through a Fourier transform:

$$\chi^{(1)}(\omega) = \int_0^\infty R^{(1)}(t') e^{i\omega t'}\, dt'. \tag{3.26}$$

Let's briefly return to the case of $\chi^{(1)}$ being non-dispersive. The inclusion of the polarization **P** on Maxwell's equations is through Eqs. (1.26) and (1.29), which now become [42, 31]:

$$\nabla \cdot (\epsilon_0 \mathbf{E} + \mathbf{P}) = 0 \tag{3.27}$$

$$\nabla \times \mathbf{B} = \mu_0 \epsilon_0 \frac{\partial \mathbf{E}}{\partial t} + \mu_0 \frac{\partial \mathbf{P}}{\partial t}. \tag{3.28}$$

Doing the same procedure as of section 1.3, we arrive at the following wave equation for **E**:

$$\nabla(\nabla \cdot \mathbf{E}) - \nabla^2 \mathbf{E} + \frac{1}{c^2} \frac{\partial^2 \mathbf{E}}{\partial t^2} = -\frac{1}{\epsilon_0 c^2} \frac{\partial^2 \mathbf{P}}{\partial t^2}. \tag{3.29}$$

This equation can be simplified: since **P** is directly proportional to **E**, Eq. (3.27) assures us that $\nabla \cdot \mathbf{E} = 0$, thus the first term of (3.29) vanishes identically, and by substituting (3.23) on the right hand side of (3.29), we find

$$\nabla^2 \mathbf{E} - \frac{1}{c^2} \frac{\partial^2 \mathbf{E}}{\partial t^2} = \frac{\chi^{(1)}}{c^2} \frac{\partial^2 \mathbf{E}}{\partial t^2}. \tag{3.30}$$

This can be further simplified by defining the refractive index n as

$$n^2 = 1 + \chi^{(1)}. \tag{3.31}$$

thus, we finally arrive at

$$\nabla^2 \mathbf{E} - \frac{n^2}{c^2} \frac{\partial^2 \mathbf{E}}{\partial t^2} = 0. \tag{3.32}$$

Equation (3.32) encapsulates that the effect of the linear polarization is to change the speed of light inside the medium to c/n. This change in the speed of light is the core of linear optics.

3.2 Nonlinear polarization

Equations (3.23) and (3.24) work well for weak fields, but fail to describe the medium's polarization when the electric field amplitude becomes comparable to the atomic fields that hold the charges together. When such strong fields act on a medium, the polarization is better described by the general power series expansion on the electric field [16]:

$$\frac{1}{\epsilon_0} \mathbf{P} = \chi^{(1)} \cdot \mathbf{E}^1 + \chi^{(2)} \cdot \mathbf{E}^2 + \chi^{(3)} \cdot \mathbf{E}^3 + \dots, \tag{3.33}$$

where $\chi^{(n)}$ represents the nth-order susceptibility (in general it is a $(n + 1)$-rank tensor for anisotropic media) and the notation $\chi^{(n)} \cdot \mathbf{E}^n$ represents the tensor contraction between the susceptibility and the electric field components. In a different notation, Eq. (3.33) is sometimes written as

$$\mathbf{P} = \mathbf{P}^{(1)} + \mathbf{P}^{(2)} + \mathbf{P}^{(3)} + \dots, \tag{3.34}$$

where $\mathbf{P}^{(n)} = \epsilon_0 \chi^{(n)} \cdot \mathbf{E}^n$ is the nth-order polarization. For dispersive media, the susceptibilities depend on the frequencies of the electric field as well, and Eqs. (3.33) and (3.34) must be analyzed in frequency domain, similar to what was done in Eq. (3.24). In general, for an incoming electric field composed of n different frequencies $\omega_1, \ldots, \omega_n$, the term $\mathbf{P}^{(n)}$ in expansion (3.34) involves a mixture of the n frequencies and therefore the susceptibility $\chi^{(n)}$ is a function of these [16]:

$$\chi^{(n)} = \chi^{(n)}(\omega_1, \omega_2, \ldots, \omega_n). \tag{3.35}$$

Just like for the linear case, the time dependent nth-order polarization can be found by defining a nth-order response tensor $\mathbf{R}^{(n)}$ and integrating over time [16]:

$$\mathbf{P}^{(n)}(t) = \epsilon_0 \int_0^\infty dt_1 \cdots \int_0^\infty dt_n \, \mathbf{R}^{(n)}(t_1, \ldots, t_n) \cdot \mathbf{E}(t - t_1) \cdots \mathbf{E}(t - t_n). \tag{3.36}$$

Equation (3.29) still holds when $\mathbf{P}$ is given by expansion (3.33), however, the term $\boldsymbol{\nabla} \cdot \mathbf{E}$ does not vanish in general. Despite this, it is usually a small term, and can be neglected [16]. Thus, the nonlinear wave equation is

$$\nabla^2 \mathbf{E} - \frac{1}{c^2} \frac{\partial^2 \mathbf{E}}{\partial t^2} = \frac{1}{\epsilon_0 c^2} \frac{\partial^2 \mathbf{P}}{\partial t^2}. \tag{3.37}$$

Notice that this equation is in the form of a wave equation with a source term on the right-hand side. Since this source term depends on powers of the electric field by Eq. (3.33), it can induce effects that oscillate at different frequencies from the incoming electric field. These effects are further divided into parametric and non-parametric processes: parametric processes conserve the energy of the electromagnetic field, examples are harmonic generation, sum and difference frequency generation, optical rectification and the intensity dependent refractive index, [16]; non-parametric processes however do not conserve the energy of the field, examples being saturable absorption and stimulated Raman scattering [16]. Instead of describing all the possible nonlinear optical processes, the focus will now be put on the third order effects, which are the ones investigated in this work.

3.2.1 Third order effects

For samples composed of gases, liquids, amorphous solids and centrosymmetric crystals, the lowest order nonlinear susceptibility is the third order term, characterized by $\chi^{(3)}$ [16]. This happens because all these materials obey inversion symmetry: inverting the sign of the incident electric field (i.e., $\mathbf{E}$ to $-\mathbf{E}$) is equivalent to inverting the sign for the emitted electric field, i.e., changing $\mathbf{P}$ to $-\mathbf{P}$. However, since the most general $\mathbf{P}(\mathbf{E})$ is given by Eq. (3.33), requiring that $\mathbf{P}(-\mathbf{E}) = -\mathbf{P}(\mathbf{E})$ implies in all even susceptibilities vanishing identically, leaving only the odd terms in expansion (3.33).

An effect of the third order susceptibility is the nonlinear refractive index. Suppose a linearly polarized, monochromatic EM field of the type (ignoring the spatial dependence)

$$E(t) = E_0 \cos(\omega t) \tag{3.38}$$

is incident on a nonlinear medium with third order polarization:

$$P(t) = \epsilon_0 \chi^{(1)} E(t) + \epsilon_0 \chi^{(3)} E(t)^3. \tag{3.39}$$

With Eq. (3.38) and using the identity $\cos(\omega t)^3 = [\cos(3\omega t) + 3\cos(\omega t)]/4$, the medium's response is

$$P(t) = \epsilon_0 \chi^{(1)} E_0 \cos(\omega t) + \frac{3}{4}\epsilon_0 \chi^{(3)} E_0^3 \cos(\omega t) + \frac{1}{4}\epsilon_0 \chi^{(3)} E_0^3 \cos(3\omega t). \tag{3.40}$$

In Eq. (3.40), there is one term that depends on 3ω, which is responsible for the third harmonic generation [16]. There are also two terms that oscillate at the original frequency of the field: the first is linear in E_0 and is responsible for the linear refractive index as already discussed; the second one depends on the third order of the field amplitude, however, due to oscillating at the same frequency it can be grouped together with the linear contribution, which motivates the definition of an *effective* susceptibility χ_{eff} as

$$\chi_{\text{eff}} = \chi^{(1)} + \frac{3}{4}\chi^{(3)} E_0^2. \tag{3.41}$$

From χ_{eff}, we can also define an effective refractive index n [16],

$$\begin{aligned} n^2 &= 1 + \chi_{\text{eff}} && (3.42) \\ &= n_0^2 \left(1 + \frac{3}{4}\frac{\chi^{(3)} E_0^2}{n_0^2}\right) && (3.43) \end{aligned}$$

where n_0 is the linear refractive index, defined as $n_0^2 = 1 + \chi^{(1)}$. The form (3.43) for the nonlinear refractive index is convenient since, typically, $\chi^{(3)} E_0^2$ is orders of magnitude smaller than n_0^2, motivating a Taylor expansion up to the lowest order in $\chi^{(3)}$ when taking the square root of Eq. (3.43):

$$n \approx n_0 \left(1 + \frac{3}{8}\frac{\chi^{(3)} E_0^2}{n_0^2}\right). \tag{3.44}$$

Through the definition of intensity, Eq. (3.20), which in a medium with linear refractive index n_0 is modified to

$$I = \frac{1}{2} n_0 \epsilon_0 c |E|^2, \tag{3.45}$$

we rewrite Eq. (3.44) to

$$n(I) = n_0 + n_2 I, \tag{3.46}$$

known as the *intensity dependent refractive index*, with n_2 defined as [16]

$$n_2 = \frac{3}{4}\frac{\chi^{(3)}}{n_0^2 c \epsilon_0}. \tag{3.47}$$

Eq. (3.46) describes the nonlinear refractive index experienced by the same beam which generated it, leading to effects such as self-focusing and self-phase modulation [16, 28]. However, in this work we are interested when one beam generates the nonlinear response and another, separate beam experiences it - this is described by the pump and probe setup. In this setup, a strong excitation (pump) beam E_e stimulates the nonlinear response of the sample, while a probe beam E_p, much weaker than the excitation ($|E_p| \ll |E_e|$), measures the change in the optical response of the sample due to the excitation. The electric field for the pump and probe setup is given by (assuming the same polarization and ignoring the spatial dependence):

$$E = E_e e^{-i\omega_e t} + E_p e^{-i\omega_p t} + \text{c.c.}\,, \tag{3.48}$$

where c.c. stands for the complex conjugate of the terms that precede it[1]. Due to the probe being much weaker than the excitation beam, the nonlinear effects due to the excitation will be much stronger than those due to the probe, therefore we can ignore the nonlinear contributions of E_p, keeping only the first order terms. For example, the nonlinear refractive index (3.46) experienced by the probe will be a function of the *pump* intensity I_e:

$$n_p = n_0(\omega_p) + n_2(\omega_p, \omega_e) I_e, \tag{3.49}$$

where the frequency dependence of each term was shown for clarity. For the non-instantaneous effects, we use Eq. (3.36) to write the third order polarization as

$$P^{(3)}(t) = \epsilon_0 \int_{-\infty}^{\infty} d\tau_1 \int_{-\infty}^{\infty} d\tau_2 \, R^{(3)}(\tau_1, \tau_2) \left| E_e(t - \tau_1 - \tau_2) \right|^2 E_p(t - \tau_1), \tag{3.50}$$

which follows from Eq. (3.36) assuming $|E_e| \gg |E_p|$. This equation will contribute with a non-instantaneous effect to n_2 as well. Since all the effects caused by the pump beam is through n_2, this is the parameter to be measured.

The inner mechanisms that produce n_2 are varied [18]: the fast electronic transitions between states, nonlinearities in glasses (doped amorphous SiO_2), semiconductor nonlinearities, molecular reorientation in liquids and gases, electrostriction and thermal nonlinearities. These mechanisms happen in different timescales, from the sub-femtosecond electronic response to the millisecond-long thermal nonlinearities [18], and thus the time resolution of the experiment is vital to resolve which mechanisms are at play.

3.2.2 Beam deflection technique

The beam deflection technique is a type of pump and probe where, as the name suggests, the measured parameter is the transversal displacement the probe beam experiences due to the nonlinearity created by the pump. Originally proposed as a technique to measure photothermal effects using CW and pulsed beams [43, 65], it has been adapted to measure the fast rotational and electronic nonlinearities [27, 61] as well. Here we are interested in the latter application of the technique.

The beam deflection technique utilizes the index gradient created by the Gaussian profile of the excitation beam to induce a small deflection on the probe beam, in a setup shown in Fig. 3.2. If the excitation spot size w_e is sufficiently bigger than the probe spot size w_p (usually, $w_e/w_p \geq 3$) and the angle between the probe and excitation is small ($< 5^\circ$), the index gradient experienced by the probe will be practically constant on the y direction and linear on the x direction. Working in the thin sample approximation (where the sample size L is significantly smaller than the Rayleigh range, $L \ll z_R$) and neglecting the nonlinear phase shift $\varphi_{\mathrm{NL}} = k_0 \Delta n_p L \ll 1$, the index gradient can be approximated as a thin prism that deflects the probe by an angle θ given by [27, 43, 65]

$$\theta(x, y, t) = \int_0^L \frac{\partial}{\partial x} n_p(x, y, z, t) \, dz \approx L \frac{\partial}{\partial x} n_p(x, y, t), \tag{3.51}$$

where the right hand side is valid in the thin sample approximation, $n_p(x, y, t)$ is the index experienced by the probe beam and the sample was assumed to be located at $z = 0$.

The refractive index n_p can be further divided into $n_p = n_{0,p} + \Delta n_p$, where $n_{0,p}$ is the constant linear refractive index and Δn_p is the change in refractive index due to the excitation. For third

---

[1] When dealing with nonlinear optical processes, we have to use the real representation of the fields, since the principle of superposition is no longer applicable when the nonlinear polarization is present.

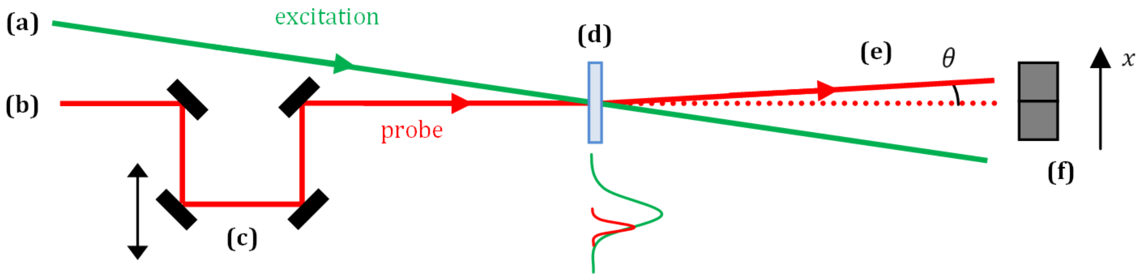

Figure 3.2: the pump and probe setup used in the beam deflection technique (adapted from [27]). (a) excitation beam; (b) probe beam; (c) delay line (used if the probe is also from a pulsed source); (d) sample, with the drawing below it showing the alignment between excitation and probe; (e) probe beam deflected by a small angle θ; (f) segmented photodiode, measuring the difference in power in the x direction.

order effects, this change is proportional to the intensity of the excitation, thus Δn_p also has a Gaussian profile:

$$\Delta n_p(x, y, t) = \Delta n_p(t) \exp\left[-\frac{2(x^2 + y^2)}{w_e^2}\right] \tag{3.52}$$

where $\Delta n_p(t)$ carries the temporal information of the index change, and is proportional to the convolution of the material response and excitation intensity [27], with the latter having a Gaussian temporal profile with τ_e HW1/eM duration [27]. Eq. (3.52) is true when the absorption of the sample is negligible. If that is not the case, heat diffusion may increase the size of $\Delta n_p(x, y, t)$, making it bigger than the spot size w_e [43]. If the absorption is negligible, the largest angle θ is realized when the probe passes the point of highest derivative at $x = w_e/2$ and $y = 0$, so by Eqs. (3.51) and (3.52)

$$\theta(t) = \frac{2L}{w_e\sqrt{e}}\Delta n_p(t). \tag{3.53}$$

Next, the probe beam propagates towards the detector located a distance z away from the sample, and the spatial profile of the intensity at the detector is given by [27]

$$I_p(x, y, z) = I_{p,0}(z) \exp\left[-2\frac{(x - \theta z)^2 + y^2}{w_p(z)}\right], \tag{3.54}$$

The detector utilized in this technique is a segmented photodiode, capable of measuring the difference in power ΔP between the right and left portions of the detector. For small deflections, this signal will be linear in the deflection $\Delta x = z\theta$, and is given by (see Chapter 4 for more details)

$$\Delta P = P \cdot \frac{4}{\sqrt{2\pi}} \frac{\theta z}{w_p(z)}, \tag{3.55}$$

where P is the total power, calculated by integrating Eq. (3.54) in the xy plane. Usually the distance z is greater than the Rayleigh range z_R ($z \gg z_R$), allowing to approximate $w_p(z) \approx w_{p,0} \cdot (z/z_R) = 2z/(k_0 w_{p,0})$ (Eqs. (3.11) and (3.12)) and thus Eq. (3.55) will be z independent:

$$\frac{\Delta P}{P} = \frac{2}{\sqrt{2\pi}} k_0 w_{p,0}\, \theta, \tag{3.56}$$

where $w_{p,0}$ is the probe minimum waist radius, $w_p(z = 0) = w_{p,0}$, and $k_0 = 2\pi/\lambda$ is the probe wavevector magnitude in vacuum.

The results (3.55) and (3.56) are independent from the mechanism that created the deflection (be it thermal, electronic or orientational nonlinearities). For the case of non-thermal nonlinearities, $\theta(t)$ is given by Eq. (3.53), and thus the signal will be

$$\frac{\Delta P}{P} = \frac{4k_0 L}{\sqrt{2\pi e}} \frac{w_{p,0}}{w_e} \Delta n_p(t). \tag{3.57}$$

If the probe comes from a pulsed laser source with τ_p pulse duration (defined as the HW1/eM), then the intensity profile (3.54) will have a temporal factor of

$$I_p(x, y, z, t - \tau_d) = I_p(x, y, z) \exp\left[-\frac{(t - \tau_d)^2}{\tau_p^2}\right] \tag{3.58}$$

where τ_d is the delay introduced by the delay line (Fig. 3.2). With the pulsed probe, the power P will also be a function of time, and therefore the normalized signal is given by the integrated power instead [27]:

$$\frac{\Delta E_p(\tau_d)}{E_p} = \frac{\int_{-\infty}^{\infty} \Delta P(t - \tau_d)\, dt}{\int_{-\infty}^{\infty} P(t - \tau_d)\, dt} = \frac{4k_0 L}{\sqrt{2\pi e}} \frac{w_{p,0}}{w_e} \langle n_p \rangle(\tau_d), \tag{3.59}$$

where $\langle n_p \rangle(\tau_d)$ is the change in refractive index averaged over the probe temporal profile, which is a function of the delay τ_d. This delay is used to distinguish the fast dynamics from the slow effects.

Through the independence between the probe and excitation beams, this technique allows to resolve the tensor elements of $\chi^{(3)}$ by using different combinations of polarization. It is even possible to measure dispersion effects by changing the wavelengths of the two beams [27].

Chapter 4

Amplification of third order optical effects with weak measurements

4.1 Experimental setup

The development of this technique began by recreating the experimental setup used by Dixon et al [23] to measure ultrasmall deflections through weak values. Their setup consisted of a Sagnac interferometer whose postselection was achieved by destructive interference at the exit of the interferometer. The displacement was imparted on the beam through a piezo-driven mirror. Through the use of the anomalous amplification the smallest deflection angle they measured was 400 frad [23]. Furthermore, their setup can be easily analyzed in both quantum and classical descriptions [23, 66], and here we will use each as a matter of convenience. This setup was then adapted as the probe beam for the beam deflection technique, with a separate excitation beam being used to create the nonlinear refractive index.

We begin by considering a collimated beam and analyze it with the quantum mechanical description of weak values. As our probe beam, we used a 633 nm HeNe laser (model Melles Griot 05-LHP-845, 15 mW of power) emitting at the fundamental TEM_{00} mode, described by a Gaussian intensity profile. The beam was made to be collimated and prepared on the diagonal polarization state before entering the interferometer (Fig. 4.1), which in the weak measurement protocol is equivalent to preparing the photons in the initial state

$$|I\rangle = |i\rangle \int dx\, \psi(x)|x\rangle = \frac{1}{\sqrt{2}}[|H\rangle + |V\rangle] \int dx\, \psi(x)|x\rangle, \tag{4.1}$$

where $\psi(x) \propto \exp(-x^2/w_p^2)$, with w_p the probe beam waist radius (constant in the case of a collimated beam).

The Sagnac interferometer was constructed with a 50:50 polarizing beam splitter (PBS) and dielectric mirrors to minimize power losses. The interferometer dimensions were 23 by 31 cm. We slightly displaced the beam from the center of the PBS, making the counter-propagating beams be distant by roughly 4 mm from each other (Fig. 4.1). This configuration allows for only one of the counter-propagating beams to interact with the excitation, while the other only passes through the sample. In nonlinear optics nomenclature, the interacting beam acts as the probe and the non-interacting one as the reference beam. We chose the $|V\rangle$ beam as the probe and the $|H\rangle$ as the reference.

A relative phase φ between the $|H\rangle$ and $|V\rangle$ states is added by placing a Babinet-Soleil compensator (BSC) inside the interferometer. The BSC is made from two birefringent wedges, one of each is movable through a micrometer, which allows for the phase φ to be continuously

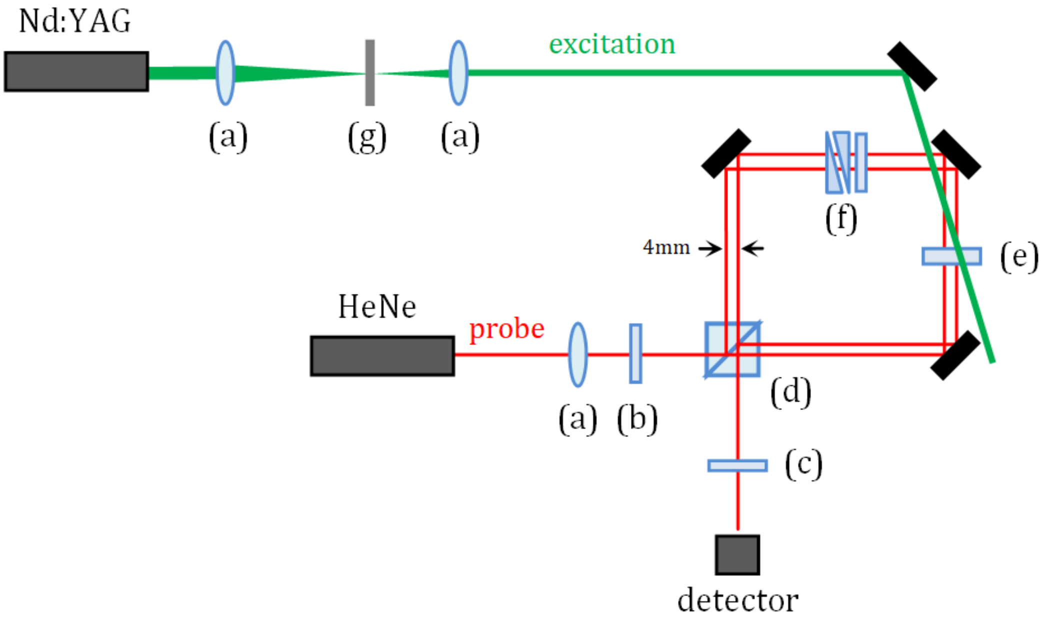

Figure 4.1: experimental setup used. (a) converging lens; (b) diagonal polarizer; (c) anti-diagonal polarizer; (d) 50:50 polarizing beam splitter; (e) sample; (f) Babinet-Soleil compensator; (g) spatial filter.

varied. Essentially then, the BSC changes the polarization state of the photons to the tunable state

$$|i\rangle = \frac{1}{\sqrt{2}}\left[|H\rangle + e^{-i\varphi}|V\rangle\right]. \tag{4.2}$$

The excitation beam was a pulsed Nd:YAG laser (model Quantel YG 781 C 20) operating at 532 nm with 8 ns pulse duration at 20 Hz repetition rate and variable pulse energy. The Nd:YAG beam was collimated through a telescope configuration shown in Fig. 4.1. We also placed a spatial filter at the focal point of the telescope, made of a hole carved by the beam on a steel blade. This spatial filter clips the higher order modes from the beam, converting it from a flat-top to a Gaussian intensity profile. At the exit of the telescope, the excitation beam retained ~50% of its input energy and had a waist radius of $w_e = (2.63 \pm 0.04)$ mm, measured through a knife-edge scan (Fig. 4.2). Whenever the pulse energy is indicated here, it corresponds to the energy after the telescope.

The probe beam was aimed to experience the nonlinear refractive index gradient induced by the excitation beam, with their alignment adjusted to impart the greatest deflection on the probe. The refractive index experienced by the probe inside the sample is written as

$$n_p = n_0 + \Delta n, \tag{4.3}$$

with n_0 being the linear refractive index and Δn the nonlinear contribution. For third order effects, Eq. (3.52) shows that Δn will also have a Gaussian spatial profile. Due to the slope of the Gaussian the probe beam is deflected by an angle θ given by Eq. (3.53). The probe beam also receives an extra phase of $k_0 \Delta n L$ due to the change in refractive index (4.3). However, we can neglect the phase from the nonlinear effects due to Δn being orders of magnitude smaller than n_0.

Ignoring absorption, the effect of the nonlinear index gradient on the probe beam can then be described as the following unitary operator

$$\hat{U} = \exp\left[-ik_0\theta\,\hat{\Pi}_V \otimes \hat{x}\right], \tag{4.4}$$

where $\hat{\Pi}_V = |V\rangle\langle V|$ is the vertical polarization projector. This unitary operator is of the same type of (2.5), which entangles the polarization state of the photon with its transverse profile by imparting a small momentum shift of $k_0\theta$ on the $|V\rangle$ polarization state and leaving the $|H\rangle$ state unchanged.

At the exit of the interferometer, both $|H\rangle$ and $|V\rangle$ polarization states were made to interfere with each other by an anti-diagonal polarizer. This polarizer acts as the postselection of the polarization states, postselecting this degree of freedom to

$$|f\rangle = \frac{1}{\sqrt{2}}(|H\rangle - |V\rangle). \tag{4.5}$$

Assuming the momentum shift $k_0\theta$ is small, we follow the same procedure to derive Eq. (2.27) and find the photon probability density to be a Gaussian with a shifted peak:

$$P_{\mathrm{wv}}(x;\theta) = |(\langle f|\langle x|)\hat{U}|I'\rangle|^2 \approx |\langle f|i\rangle|^2 |\psi(x + k_0\theta\langle\hat{\Pi}_V\rangle_{\mathrm{w}} w_p^2/2)|^2. \tag{4.6}$$

From Eqs. (4.2), (4.4) and (4.5), we can calculate

$$|\langle f|i\rangle|^2 = \sin(\varphi/2)^2 \tag{4.7}$$

$$\langle\hat{\Pi}_V\rangle_{\mathrm{w}} = -\frac{1}{2}\left(1 - i\cot(\varphi/2)\right). \tag{4.8}$$

As already explained in Chapter 2, only the imaginary part of the weak value (4.8) will be measurable in the x representation. Then, the displacement Δx of the probability density $|\psi(x)|^2$ is

$$\Delta x = \frac{1}{4}k_0\theta w_p^2 \cot(\varphi/2). \tag{4.9}$$

In practice, however, we have to take into account the propagation effects of the probe beam. That is because our probe waist radius w_p was not considerably smaller than the excitation waist w_e. To achieve the condition $w_p/w_e < 1/3$, we placed a converging lens with a focal distance of 75 cm before the PBS and made the focal point be inside the interferometer. For this converging beam, we model the propagation effects using the Fourier optics method from section 3.1 with a classical description of the fields. Suppose the sample is located at $z = 0$ and working in the thin sample approximation, the nonlinear refractive index induces a momentum shift of $g \approx k_0\theta$ on the beam. That is, the electric field amplitude in reciprocal space $E_p(p_x, p_y)$ is shifted in the x direction to $E_p(p_x + k_0\theta, p_y)$. Propagation towards the detector located at a distance z gives for the probe amplitude E_p

$$\begin{aligned} E_p &= \frac{1}{2\pi}\int E(p_x + k_0\theta, p_y)\exp\left(\frac{-ip^2 z}{2k_0}\right) e^{ip_x x + ip_y y}\, d^2p \\ &= \frac{E_0\, w_0^2}{w_0^2 + 2iz/k_0}\exp\left[-\frac{ik_0\theta^2 w_0^2 z}{2w_0^2 + 4iz/k_0} - \frac{ik_0\theta w_0^2 x}{w_0^2 + 2iz/k_0} - \frac{r^2}{w_0^2 + 2iz/k_0}\right], \end{aligned} \tag{4.10}$$

where $E(p_x, p_y) \propto \exp(-w_0^2 p^2/4)$ and $w_0 = w_p(0)$. With some algebraic manipulation, we can rewrite the exponential in Eq. (4.10) into a more convenient form

$$\exp\left[-ik_0\theta x - \frac{(x + \theta z)^2 + y^2}{w_0^2 + 2iz/k_0}\right]\exp\left[-\frac{ik_0\theta^2 w_0^2 z}{2w_0^2 + 4iz/k_0} + \frac{(\theta z)^2}{w_0^2 + 2iz/k_0}\right]. \tag{4.11}$$

Equation (4.11) is more convenient since it separates the z independent phase $-k_0\theta x$, which is the phase to be amplified, from the other phase terms. Likewise, it allows the θ^2 and $z\theta$ terms in Eq. (4.11) to be neglected, since the deflection angle θ is small ($\leq 10^{-5}$ rad) and provided θz is not too large compared to the Rayleigh range. Thus, the probe beam at the detector is approximately

$$E_p \approx \frac{E_0\, w_0^2}{w_0^2 + 2iz/k_0} \exp\left[-ik_0\theta x - \frac{x^2+y^2}{w_0^2 + 2iz/k_0} \right]. \tag{4.12}$$

The horizontally polarized reference beam E_r only undergoes free propagation by the same distance z, since it does not experience the gradient created by the excitation. We also ignored the linear phase $k_0 n_0 L$ since both beams experience it. Thus, taking into account the phase φ added due to the BSC, the intensity at the detector is given by

$$\begin{aligned} I_d &= \frac{1}{2}\epsilon_0 c |E_r - e^{-i\varphi} E_p|^2 \\ &\approx I_0 \left(\frac{w_0}{w_p(z)}\right)^2 \left|1 - e^{-ik_0\theta x - i\varphi}\right|^2 \exp\left[\frac{-2(x^2+y^2)}{w_p(z)^2}\right]. \end{aligned} \tag{4.13}$$

Since $k_0\theta$ is small, the intensity (4.13) approximately describes a Gaussian but with a smaller amplitude and shifted peak. The same displacement from Eq. (4.9) can be calculated by expanding $e^{-ik_0\theta x}$ up to first order in θ:

$$\begin{aligned} \left|1 - e^{-ik_0\theta x - i\varphi}\right|^2 &\approx \left|1 - (1 - ik_0\theta x)e^{-i\varphi}\right|^2 \\ &= 4\sin(\varphi/2)^2 \left|1 + \frac{k_0\theta x e^{-i\varphi/2}}{2\sin(\varphi/2)}\right|^2. \end{aligned} \tag{4.14}$$

Assuming the term inside the absolute square in (4.14) is nearly unity, we can reexponentiate:

$$\left|1 + \frac{k_0\theta x e^{-i\varphi/2}}{2\sin(\varphi/2)}\right|^2 \approx \left|\exp\left(\frac{k_0\theta x e^{-i\varphi/2}}{2\sin(\varphi/2)}\right)\right|^2 = \exp\left(k_0\theta x \cot(\phi/2)\right). \tag{4.15}$$

Therefore, the intensity at the detector is approximated by

$$I_d \approx I_{0d} \sin(\varphi/2)^2 \exp\left[-2\frac{(x-\Delta x)^2 + y^2}{w_p(z)^2}\right] \tag{4.16}$$

where

$$\Delta x = \frac{1}{4} k_0 \theta w_p(z)^2 \cot(\varphi/2) \tag{4.17}$$

is the shift in the peak of the Gaussian and

$$I_{0d} = 4 I_0 e^{w_p^2 (\Delta x)^2/8} \left(\frac{w_0}{w_p(z)}\right)^2. \tag{4.18}$$

The probe beam had a waist of $w_p(z) = (682 \pm 5)$ μm, measured through a knife-edge scan at the same position as the detector, with a distance z of roughly 90 cm (Fig. 4.2), measured from the focal point (located inside the sample). From those values, we also estimated a waist of $w_{p,0} = 260$ μm at the focal point.

In a realistic experimental scenario, the interferometer is subject to losses due to scattering, misalignment and background noise. These effects may result in less than ideal amplification due to the reduced contrast between the bright (diagonal polarization) and dark (anti-diagonal)

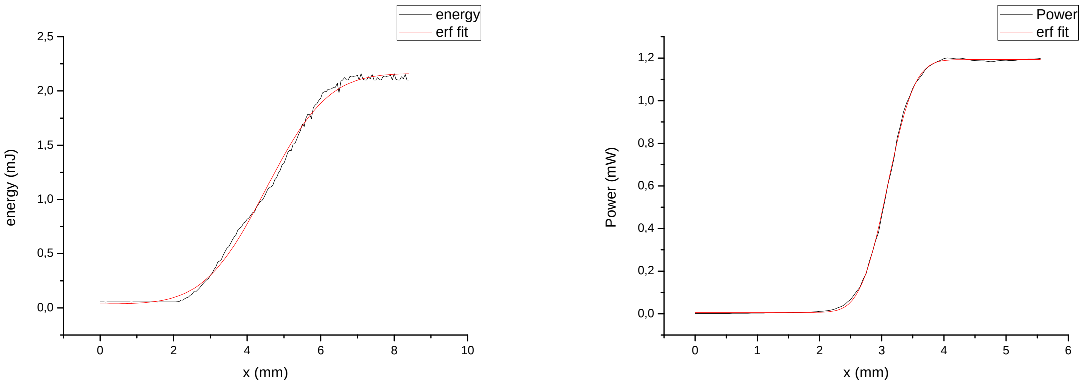

Figure 4.2: knife-edge scans of the excitation beam (left) and probe beam (right). For the excitation beam, the knife-edge scan was made after the spatial filter and telescope, which also served as a quality control of our spatial filtering. By fitting an erf function, we measured a waist of $w_e = (2.63 \pm 0.04)$ mm and $w_p = (682 \pm 5)$ μm for the excitation and probe beams, respectively. The distance z in $w_p(z)$ was measured as 90 cm from the focal spot to the detector.

exits, and we can phenomenologically include them by modifying Eq. (4.13) by including the interferometric parameter η [70]:

$$I'_d \propto \left|1 - \eta e^{-ik_0\theta x - i\varphi}\right|^2 \exp\left[\frac{-2(x^2+y^2)}{w_p(z)^2}\right]. \tag{4.19}$$

The parameter η represents the relative amplitude between each path at the exit of the interferometer, and therefore it is bounded by $0 \leq \eta \leq 1$. The contrast of the dark exit is defined as the ratio between the minimum and maximum intensities at the dark and bright ports respectively, and in our case is given by[1]

$$\frac{I_{\text{min}}}{I_{\text{max}}} = \left(\frac{1-\eta}{1+\eta}\right)^2. \tag{4.20}$$

In our experiment, the bright exit typically has a power of 5.61 mW, while the dark exit goes as low as 20 μW, thus from Eq. (4.20) we expect $\eta \approx 0.89$.

In this non-ideal scenario, the shift $\Delta x'$ is calculated through

$$\Delta x' = \frac{1}{\mathcal{N}} \int x I'_d \, dx \, dy, \tag{4.21}$$

where $\mathcal{N}$ is a normalization factor, $\mathcal{N} = \int I'_d \, dx \, dy$. Calculation of Eq. (4.21) for small θ yields

$$\Delta x' \approx \frac{k_0 \theta w_p(z)^2}{2} \frac{\eta \sin(\varphi)}{\eta^2 + 1 - 2\eta\cos(\varphi)}. \tag{4.22}$$

In the case of a perfect interferometer, $\eta \to 1$ and Eq. (4.22) reduces to Eq. (4.17), as expected.

---

[1] Typically in interferometric experiments the parameter that measures the quality of the interferometer is the visibility V, defined in terms of the maximum and minimum intensities as $V = (I_{\text{max}} - I_{\text{min}})/(I_{\text{max}} + I_{\text{min}})$. The parameter η used here is defined in terms of the relative *amplitudes* in each arm, $\eta = (E_{\text{max}} - E_{\text{min}})/(E_{\text{max}} + E_{\text{min}})$, and is therefore connected to the visibility by

$$V = \frac{2\eta}{1+\eta^2}.$$

As the detector, we used a quadrant detector (model QP50-6-18U-SD2) coupled to a oscilloscope (model Tektronix 2022B, 200 MHz bandwidth) to measure the shift $\Delta x'$. The quadrant detector has the advantage of simultaneously measuring both the sum and the difference in power between the left and right portions (in the x direction) of the detector. From these two measurements, we can calculate the relative difference in power:

$$\frac{\Delta P}{P} = \frac{P_{\text{right}} - P_{\text{left}}}{P_{\text{right}} + P_{\text{left}}}. \tag{4.23}$$

Using equations (3.21) and (3.22) for a Gaussian beam displaced by $\Delta x'$ on the x direction, Eq. (4.23) becomes

$$\begin{aligned}\frac{\Delta P}{P} &= \frac{2}{\pi w_0^2 I_0}\left[\int_0^{\infty} dx \int_{-\infty}^{\infty} dy\, I(x-\Delta x', y, z) - \int_{-\infty}^{0} dx \int_{-\infty}^{\infty} dy\, I(x-\Delta x', y, z)\right] \\ &= \operatorname{erf}\left(\frac{\sqrt{2}\Delta x'}{w_p(z)}\right),\end{aligned} \tag{4.24}$$

where we used the error function, defined as

$$\operatorname{erf}(x) = \frac{2}{\sqrt{\pi}}\int_0^x e^{-t^2}dt. \tag{4.25}$$

In Eq. (4.24) was assumed that the beam diameter $2w_p(z)$ is smaller than the detector dimensions, which is a condition satisfied by our beam. For small x, $\operatorname{erf}(x) \approx 2x/\sqrt{\pi}$, then, (4.24) reduces to

$$\frac{\Delta P}{P} = \frac{4}{\sqrt{2\pi}}\frac{\Delta x'}{w_p(z)}. \tag{4.26}$$

Inserting the displacement $\Delta x'$ of Eq. (4.22) and the deflection angle θ given by Eq. (3.53) we arrive at

$$\frac{\Delta P}{P} = \frac{4k_0 L}{\sqrt{2\pi e}}\frac{w_p(z)}{w_e}\Delta n(t)\frac{\eta\sin(\varphi)}{\eta^2+1-2\eta\cos(\varphi)}. \tag{4.27}$$

Comparing Eq. (4.27) with the standard beam deflection signal (3.57), we notice two major differences: the weak value amplification through the φ-dependent terms and a z-dependence in the spot size w_p. This can be more easily seen by rewriting (4.27) as

$$\left(\frac{\Delta P}{P}\right)_{\text{WV}} = \left(\frac{\Delta P}{P}\right)_{\text{BD}}\sqrt{1+(z/z_R)^2}\, f_\eta(\varphi) \tag{4.28}$$

where $(\Delta P/P)_{\text{BD}}$ is the standard beam deflection signal (3.57) and

$$f_\eta(\varphi) = \frac{\eta\sin(\varphi)}{\eta^2+1-2\eta\cos(\varphi)} \tag{4.29}$$

is the phase-dependent amplification factor.

The signal (4.28) turns out to be z-dependent due to the deflection only appearing in the interference between probe and reference beams, with the phase term $e^{-ik_0\theta x}$ being the responsible for this spatial imbalance. Provided $z\theta \ll z_R$, the diffraction effects will only make this interference further from the center due to the increasing beam waist $w_p(z)$ (Fig. 4.4). For the second difference, we remark that the amplification is limited by the parameter η, as can be

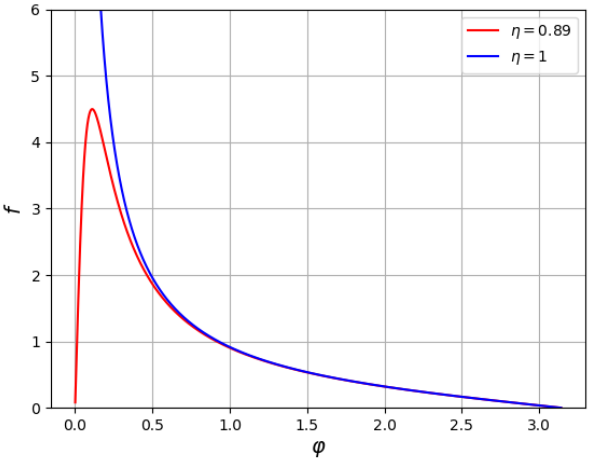

Figure 4.3: graph of the amplification factor $f_\eta(\varphi)$ from Eq. (4.29) for the values $\eta = 0.89$ (in red) and $\eta = 1$ (in blue). For the ideal case of $\eta = 1$, $f_\eta(\varphi) = \frac{1}{2}\cot(\varphi/2)$. In the non-ideal case, the amplification is limited for small φ.

seen by plotting the amplification factor $f_\eta(\varphi)$ as a function of the phase φ, Fig. 4.3. We now estimate how high the amplification factor

$$\mathcal{A} = \sqrt{1 + (z/z_R)^2}\, f_\eta(\varphi) \tag{4.30}$$

can be achieved with our current implementation. For the value $\eta = 0.89$, $f_\eta(\varphi)$ can be as great as 4.2 at $\varphi \sim 0.1$ (only the values $0 \leq \varphi < 1$ are used, since this is the interval where $f_\eta(\varphi) > 1$). For the z/z_R term, using the measured values $w_p(z) = 682$ μm and $z = 90$ cm we can calculate a divergence angle $\delta = w_p(z)/z = 760$ μrad, and from the divergence angle estimate the $w_{p,0} = 260$ μm and $z_R = 111$ mm, which gives $\sqrt{1 + (z/z_R)^2} \sim 8.1$. Thus, our current amplification factor is of the order of $\mathcal{A} \sim 34$.

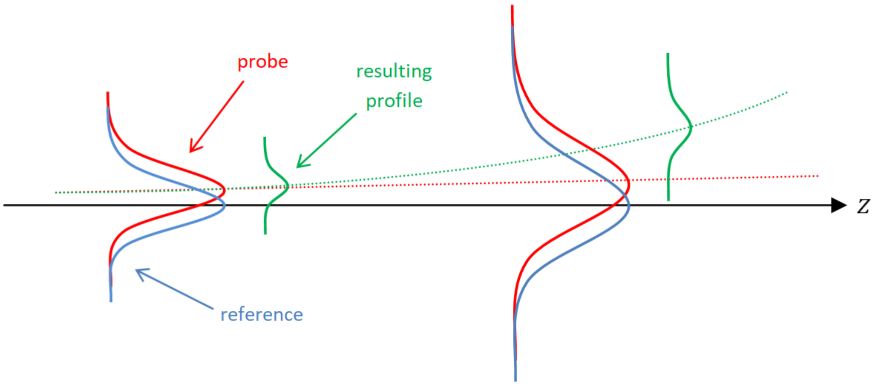

Figure 4.4: schematic showing the deflected beam (probe) intensity profile relative to the unchanged beam (reference) profile in the z axis. The green profile represents the result of the interference of the previous two beams. As the beams propagate to the right, their waist increase and more constructive interference happens further away from the z axis, resulting in a profile (green) displaced with a z^2 behavior (dotted green line), in stark contrast to the probe with its displacement linear in z (dotted red line).

The quadrant detector however was only capable of acquiring the slow response of the sample due to its 1 microsecond temporal resolution. To measure the fast response, we employed a 90º prism and two Thorlabs DET210 detectors with a 1 nanosecond rise time, which is sufficiently fast to follow the shape of the excitation pulse. The prism splits the intensity I'_d in half and sends each half to one of the fast detectors (Fig. 4.5). An electronic subtraction is performed after acquisition, which gives the difference in power ΔP. Since the DET210 sensors can only measure changes in power, the total power P had to be inferred by modulating the 633 nm beam with a chopper and varying the value of the relative phase φ. This same chopper is used to position the prism such that each detector receives the same amount of power from the probe beam when there is no excitation. In conjunction with the DET210 sensors, we used a SRS SR445A amplifier, which amplified the signal by 19 times at 50 Ω impedance and by 27 times at 500 Ω impedance.

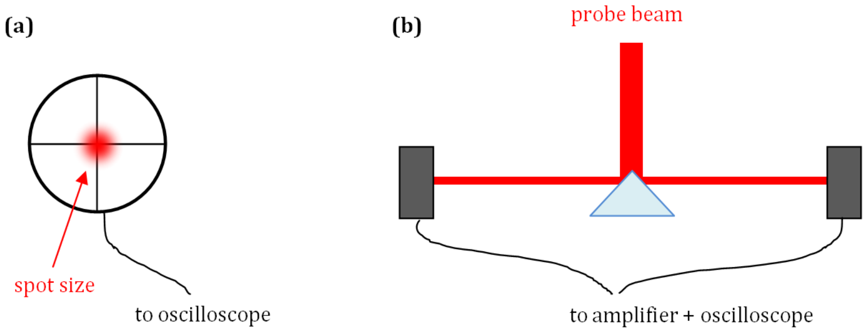

Figure 4.5: (a) front view of the quadrant detector and (b) top view of the construction used to measure the fast response with the DET210 detectors.

4.2 Results

4.2.1 OG515

The first sample we investigated was the Schott Optical Filter OG515. This is a longpass filter (see Fig. 4.6) made of glass doped with semiconductor quantum dots (QDs) of CdS_xSe_{1-x} with $x = 0.08$ and 2.8 nm crystallite diameter [8, 11]. Due to the QDs structure, the nonlinear optical properties of the semiconductor are greatly enhanced relative to the bulk case near the band gap [18], with a strong absorption for wavelengths shorter than the gap wavelength (half transmittance at 515 nm [56]). For the OG515 filter, Z-scan measurements near the band gap show a nonlinear refractive index of $n_2 = -5.7 \times 10^{-9}$ cm^2/MW at 527 nm with 4 ps pulse duration [11], which is 4 orders of magnitude larger than the typical $n_2 \sim 10^{-13}$ cm^2/MW bulk semiconductors exhibit [18].

Our first measurements on this filter used the quadrant detector and an average over 128 pulses through the oscilloscope built-in average acquisition. We started with an average post-filter excitation energy of 1.3 mJ per pulse with a repetition rate of 20 Hz. A subtraction of the Nd:YAG lamp discharge noise was performed by blocking the excitation beam and recording the detected noise to the oscilloscope reference memory, the subtraction was then performed in a LABVIEW VI. With the excitation unblocked, the phase φ was tuned away from zero and a signal was detected in the oscilloscope. The probe and excitation beams were aligned in a manner to maximize the detected signal, which corresponds to the point of the highest refractive

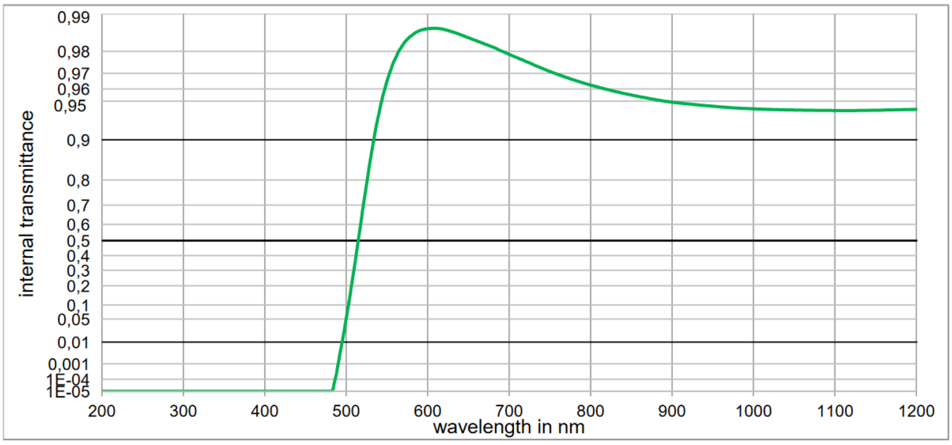

Figure 4.6: internal transmittance versus wavelength for the OG515 filter, taken from the data sheet [56]. For wavelengths near the band gap (the sharp drop in transmittance around 500 - 600 nm), the nonlinear optical properties are enhanced [18].

index gradient in the sample. With one channel of the oscilloscope recording the difference in power ΔP and the other recording the total power P, the LabVIEW VI calculated the signal $\Delta P/P$ of Eq. (4.27).

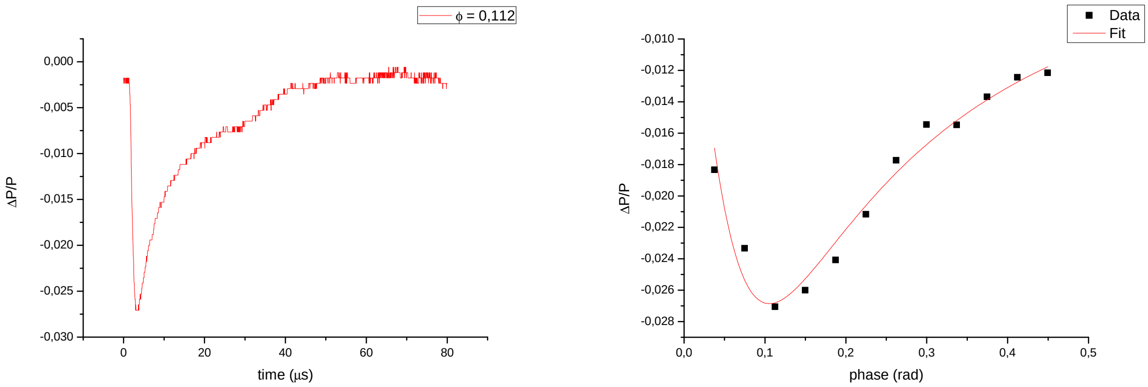

Figure 4.7: measurement of $\Delta P/P$ versus time for the phase $\varphi = 0.112$ rad (left) and peak value of $\Delta P/P$ versus phase φ (right) for 1.3 mJ pulse energy (1.53 $\mathrm{MW/cm^2}$ peak intensity) and 20 Hz repetition rate. The experimental data on the right graph correspond to the peak value of $\Delta P/P(t)$, and show the expected phase dependency of Eq. (4.27) (fitted in red) when the phase is varied.

Fig. 4.7 shows an example of the time dependency of the signal and its dependency on phase φ. Since the filter had a thickness of $L = 2.5$ mm, by fitting Eq. (4.27) on the $\Delta P/P$ versus φ graph we found $\Delta n = -8.12 \times 10^{-7}$ for the peak value in the refractive index change. Comparing our measured index change to the estimated $\Delta n = 2n_2 I_e \approx -1.4 \times 10^{-8}$ using $n_2 = -5.7 \times 10^{-9}\ \mathrm{cm^2/MW}$ [11] and a peak excitation intensity of $I_e = 1.53\ \mathrm{MW/cm^2}$, we see that our measured value is 1-2 orders of magnitude larger than the estimated one. This larger value can be due to a combination of electrostriction effects, with a typical timescale of nanoseconds - which is on the same timescale as our pulse of 8 ns - with thermal effects, on a microseconds timescale. To investigate the thermal dependency of our signal, we performed measurements to compare the signals under different repetition rates with an average pulse energy of 2.5 mJ. We tested for 20, 10 and 4 Hz which was adjusted in the Nd:YAG laser itself. From Fig. 4.8, we see a dependence on the repetition rate, especially in the long time behavior of the signal.

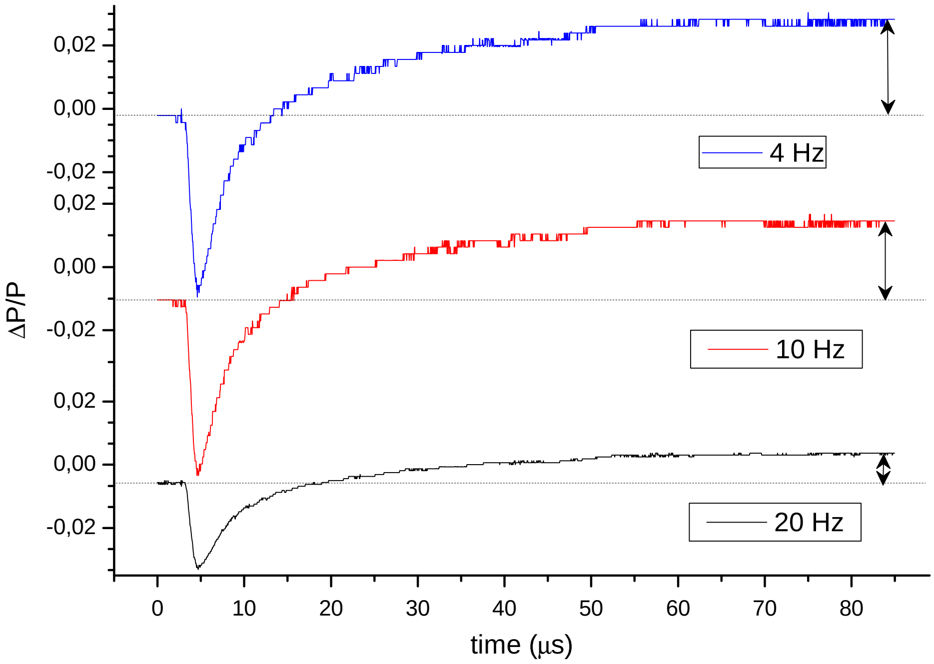

Figure 4.8: measured signal for the phase $\varphi = 0.19$ rad with 20, 10 and 4 Hz repetition rates. Pulse energy of 2.55 mJ.

We are sure these signals are all a result of the interaction between probe and excitation since by aiming the excitation away from the probe, the signal vanishes. Another condition that identifies a beam deflection signal is whether it changes signal (from positive to negative or vice-versa) when the probe is swept over the excitation spatial profile. Since the deflected signal depends on the spatial derivative of the excitation, it will invert its sign as the probe is swept over the gaussian profile of the excitation, which has a derivative proportional to $x \exp(-2x^2/w_e^2)$.

Even though the measurements with different repetition rates indicate a kind of thermal response, it was not possible to entirely resolve the thermal effects from the non-thermal ones due to the quadrant detector $\sim 1\ \mu$s response. With this in mind, we replaced the quadrant detector with the 1 ns rise time DET210 detectors. We expected these detectors would be able to distinguish the fast, nanosecond effects from the slow ones, and indeed we observed effects on dozens of nanoseconds. However, the observed signal did not behave like in the previous detector. The signal in both channels (with each corresponding to one DET210 detector) shows its largest value when $\varphi = \pi$ (Fig. 4.9), in contrast to the weak valued signal that shows its peak at φ close to 0. Even by subtracting both channels to get ΔP, no signal is observed since both detectors see the same variation.

The fact both detectors measured the same signal, we suspect we have observed a type of saturable absorption. With the presence of the excitation pulse, the sample absorbs a fraction of the probe power, creating a homogeneous change in intensity that both detectors see. This is also befitting with the largest signal being observed at $\varphi = \pi$, since in the case of absorption the intensity at the detectors can be written as

$$I_d \propto |1 - A(t)e^{-i\varphi}|^2 = 1 + A(t)^2 - 2A(t)\cos\varphi, \tag{4.31}$$

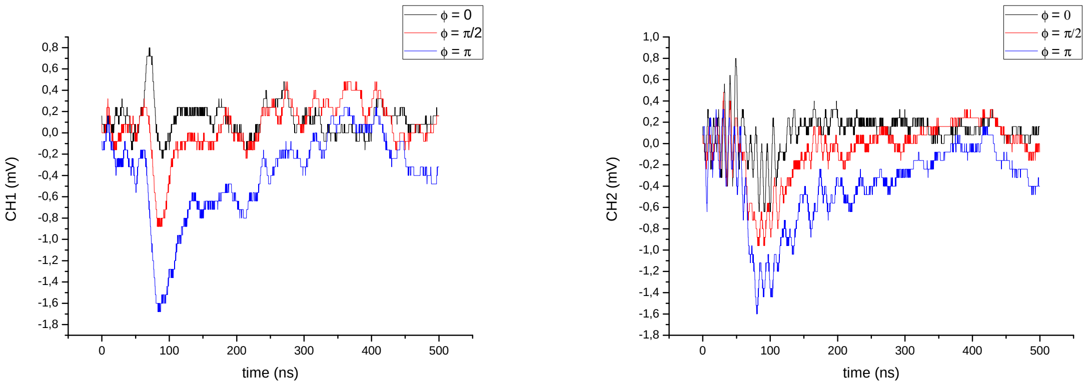

Figure 4.9: measured signals for the phases $\varphi = 0$, $\pi/2$ and π by the left and right DET210 detectors. Pulse energy of 10 mJ.

where $A(t)$ is the variable amplitude due to absorption and the displacement of the beam was ignored for simplicity.

4.2.2 Acetone

Acetone ($CH_3(CO)CH_3$) is a a liquid at room temperature and a typical solvent for chemical reactions. In order to distinguish the nonlinear response of the solute from the solvent, it is imperative to characterize the latter in similar scenarios. Being a molecular liquid, acetone shows two major contributions to its nonlinear response: the fast bound-electronic contribution and the nuclear contributions [18, 72]. With the pulse width used in this work, the bound-electronic response can be treated as instantaneous, and their contribution to Δn is equal to $2n_{2,el}I_e(t)$ [72], where $n_{2,el}$ is the n_2 value due to the bound electrons. Now for the nuclear contributions, they arise from the diffuse molecular reorientation (where the induced dipole aligns to the excitation field), molecular libration, collision and vibration [18, 72]. These nuclear contributions are generally non-instantaneous, and when taken into account in Δn through Eq. (3.50) it becomes [72]

$$\Delta n = 2n_{2,el}I_e(t) + \sum_j n_{2,j} \int_{-\infty}^{\infty} dt'\, r_j(t-t')I_e(t') \tag{4.32}$$

where $r_j(t-t')$ is a normalized response function and j indexes the different nuclear contributions (diffuse reorientation, libration, etc). The response function typically induces an exponential rise and fall to the time resolved measurement [72].

In our first measurements, we used the quadrant detector already introduced. With this steup, we measured a modulation of the signal in the scale of microseconds. This modulation is practically the same for both repetition rates of 20 and 5 Hz (Fig. 4.10), and its amplitude increased with phase φ similar to the weak value amplification term. However, the figure does not properly show the exponential rise and fall expected in molecular liquids.

Once again we attempted to measure the fast response by employing the DET210 sensors, however no signal was observed with them - not even a sign of saturable absorption. Our initial attempts used excitation energies in the 1-3 mJ range, and later we increased to around 25 mJ and even focalized the excitation beam close to the sample in an attempt to increase the signal, but nothing was observed as well. With this lack of results we were led to believe the prism and fast detectors are not able to replicate the same behavior as the quadrant detector for this type of measurement.

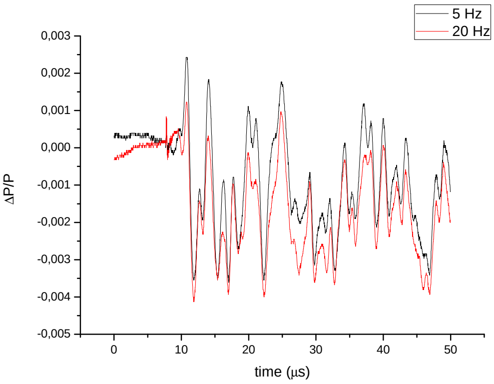

Figure 4.10: measured signal in acetone comparing the different repetition rates for the phase $\varphi = 0.1$ rad and pulse energy 1.3 mJ.

The next step in development is to measure the fast response of the samples. We plan to achieve that by replicating this technique using a mode-locked Ti:sapphire laser system available in another laboratory in our group, which delivers pulses of 120fs at a repetition rate of 78MHz. The pulsed laser compensates the lack of temporal resolution and its wavelength of 780 nm has an optimal spectral response by the quadrant detector. Using this laser, we expect to make measurements similar to the time-averaged signal (3.59) but with the benefits from the weak-valued procedure already discussed in this chapter.

Concluding remarks

Weak measurements have received increased attention in the last decade as a novel metrological tool for measuring small parameters. From a fundamental perspective, weak measurements exploit the non-separability introduced by an interaction that entangles two degrees of freedom, with a destructive interference between quantum states postselecting the system onto a state that shows an amplified effect of such interaction. This amplification property of the weak value can be used to improve the signal-to-noise ratio (SNR) in many situations, outperforming conventional techniques [17]. Weak values also found fundamental quantum applications, from steering quantum systems [46] to raising questions about the interpretation of fundamental properties [3, 21]. But as explained in text, the properties underlying weak measurements are more general, and they can also be realized with purely classical systems, which motivated a more general review of the underlying features of both quantum mechanics and classical optics.

Starting from a revision of vector spaces, we showed how the concept of non-separability emerges from the mathematical structure of quantum mechanics and classical optics, which serves as a motivation for the recent developments in the quantum-classical boundary. The non-separability allows for entanglement-like correlations to be observed with classical entities, such as state teleportation [33] and Bell-like inequalities violations [29]. This all comes with the benefit of the robustness classical experiments have against environment perturbations, creating reliable tabletop measurements that can achieve great precision and fidelity.

The second half of this work focused on applying a weak-valued procedure to the beam deflection (BD) technique. The BD technique is a type of pump-and-probe where the probe beam is deflected by the index gradient created by the excitation, and it is versatile enough to measure thermal and non-thermal nonlinearities [27, 43, 61, 65, 72]. In our proposal, we applied this deflection inside a Sagnac interferometer, which coupled the deflection to the polarization state of the probe beam. With a polarizer set at an almost orthogonal orientation to the initial polarization of the probe, a large signal can be observed due to the weak-valued amplification. Besides this latter amplification, we also found the signal to depend on the probe's spot size at the detector, and not at the focal point like the conventional BD technique. The dependence with the variable spot size is another byproduct of the interferometric aspect of our signal, opening another possibility to improve the SNR. When both amplification mechanisms are accounted for, we found an amplification factor $\mathscr{A} \sim 34$ when compared to the usual implementation of the BD technique.

Our experimental implementation of the weak-valued BD technique used a CW 633 nm HeNe laser as the probe and a pulsed (8 ns temporal width) 532 nm Nd:YAG laser as the excitation, together with a quadrant detector. With this setup we could promptly detect thermal response on the OG515 glass filter, but due to using a CW beam as the probe we did not achieve the temporal resolution necessary to reliably detect non-thermal effects (such as electronic nonlinearities). We also tried employing two fast (ns rise time) sensors with a 90º prism to split the beam, however this approach did not work like the quadrant detector and was only able to measure a type of saturable absorption. The same procedure was applied to acetone, however the current implementation led to inconclusive results.

Due to COVID restrictions, we were not able to modify our implementation to a pulsed (fs pulse width) Ti:Sapphire laser, which would provide the necessary temporal resolution for non-thermal measurements. In the future, we expect to use this new laser source to experimentally demonstrate an improvement in the detection of small nonlinearities. For instance, the amplification factor $\mathcal{A}$ can be as high as $\mathcal{A} \sim 80$ for $\eta = 0.94$ and $z/z_R \sim 10$, which should be achievable with our current equipment. There are still many possibilities to implement classical non-separability yet to be explored (for instance, last year a polarization-frequency non-separability was explored by Kopf et al. [45]), and this topic has a very broad applicability suited for theoretists and experimentalists alike.

Appendix A

Fisher information and the Cramér-Rao bound

A.1 Fisher information

Consider estimating an unknown parameter g from a set $\mathbf{x} = \{x_1, x_2, \ldots, x_N\}$ of N independent measurements of a random variable X, described by a probability distribution $P(x; g)$ [53, 60]. The Fisher information is a measure of how much information about the parameter g is available in the set $\mathbf{x}$ [22]. We first introduce the likelihood function $P(\mathbf{x}; g)$, defined as the probability to measure the string $\mathbf{x}$ of values:

$$P(\mathbf{x}; g) = \prod_{i=1}^{N} P(x_i; g). \tag{A.1}$$

From the likelihood function, the score $V(\mathbf{x}; g)$ describes its sensitivity to changes in the parameter g, and it is defined as

$$V(\mathbf{x}; g) = \frac{\partial}{\partial g} \ln P(\mathbf{x}; g) = \sum_{i=1}^{N} \frac{\partial}{\partial g} \ln P(x_i; g) = \sum_{i=1}^{N} V(x_i; g) \tag{A.2}$$

where the score of each measurement $V(x_i; g)$ was defined as $V(x_i; g) = \partial_g \ln P(x_i; g)$.

The Fisher information $F_N(g)$ is defined as the variance of the score [22, 53],

$$F_N(g) = \mathrm{Var}[V(\mathbf{x}; g)]. \tag{A.3}$$

Assuming $P(x_i; g)$ is normalized and with a few regularity conditions [22], it can be shown that the expectation value (denoted here as E[ ]) of the score of each measurement $V(x_i; g)$ has zero mean:

$$\mathrm{E}[V(x_i; g)] = \int \left(\frac{1}{P(x_i; g)} \frac{\partial P(x_i; g)}{\partial g} \right) P(x_i; g)\, dx_i = \frac{\partial}{\partial g} \int P(x_i; g)\, dx_i = 0 \tag{A.4}$$

since $P(x_i; g)$ is normalized. And since the expectation value is a linear operator, $\mathrm{E}[V(\mathbf{x}; g)] = 0$ as well.

From Eqs. (A.3) and (A.4), we can rewrite the Fisher information as

$$\begin{aligned} F_N(g) &= \mathrm{Var}[V(\mathbf{x};g)] = \mathrm{E}\left[V(\mathbf{x};g)^2\right] \\ &= \int V(\mathbf{x};g)^2 P(\mathbf{x};g)\, dx_1\cdots dx_N \\ &= \int \frac{1}{P(\mathbf{x};g)}\left(\frac{\partial P(\mathbf{x};g)}{\partial g}\right)^2 dx_1\cdots dx_N \qquad \text{(A.5)} \\ &= -\int \left(\frac{\partial^2}{\partial g^2}\ln P(\mathbf{x};g)\right) P(\mathbf{x};g)\, dx_1\cdots dx_N = -\mathrm{E}[\partial_g V(\mathbf{x};g)] \qquad \text{(A.6)} \end{aligned}$$

Using the definition (A.6), we can see that the Fisher information F_N is additive over independent trials: from the definition of score (A.2),

$$F_N(g) = -\mathrm{E}[\partial_g V(\mathbf{x};g)] = -\mathrm{E}\left[\partial_g \sum_{i=1}^{N} V(x_i;g)\right] = -\sum_{i=1}^{N} \mathrm{E}\left[\partial_g V(x_i;g)\right]. \qquad \text{(A.7)}$$

Since the measurements are all independent from each other, the expectation values inside the summation (A.7) will all be equal to $-F(g)$, the Fisher information of a single measurement. Therefore,

$$F_N(g) = NF(g), \qquad \text{(A.8)}$$

proving that the Fisher information over N independent measurements is additive.

A.2 Cramér-Rao bound

In order to derive the Cramér-Rao bound, we must go back to our unbiased estimator $\hat{g}(X)$ of Chapter 2. By the definition of an unbiased estimator, the following equality holds for whatever value of g:

$$\mathrm{E}\left[\hat{g}(X) - g\right] = \int (\hat{g}(x) - g)\, P(x;g)\, dx = 0. \qquad \text{(A.9)}$$

By taking a derivative of (A.9) with respect to g, its result must also be zero. Thus

$$\frac{\partial}{\partial g}\int (\hat{g}(x) - g)\, P(x;g)\, dx = \int (\hat{g}(x) - g)\,\frac{\partial P}{\partial g}\, dx - \int P(x;g)\, dx = 0. \qquad \text{(A.10)}$$

Using the following identity

$$\frac{\partial P}{\partial g} = P\frac{\partial \ln P}{\partial g} \qquad \text{(A.11)}$$

together with the fact that $P(x;g)$ is normalized, $\int P\, dx = 1$, Eq. (A.10) becomes

$$\int (\hat{g} - g) P \frac{\partial \ln P}{\partial g}\, dx = 1. \qquad \text{(A.12)}$$

Now, assuming the probability distribution P is sufficiently smooth, we can factor the integrand of (A.12) as

$$\int \left((\hat{g} - g)\sqrt{P}\right)\left(\sqrt{P}\frac{\partial \ln P}{\partial g}\right) dx = 1, \qquad \text{(A.13)}$$

Squaring the expression (A.13), we can invoke the Cauchy-Schwarz inequality:

$$1 = \left[\int \left((\hat{g} - g)\sqrt{P}\right)\left(\sqrt{P}\frac{\partial \ln P}{\partial g}\right) dx\right]^2 \leq \left[\int (\hat{g} - g)^2 P\, dx\right]\left[\int \left(\frac{\partial \ln P}{\partial g}\right)^2 P\, dx\right]. \tag{A.14}$$

We recognize the term inside the first brackets of (A.14) as the variance of the estimator g, while the second bracketed term is recognized as the Fisher information $F(g)$:

$$F(g) = \int \left(\frac{\partial \ln P}{\partial g}\right)^2 P\, dx = \int \frac{1}{P}\left(\frac{\partial P}{\partial g}\right)^2 dx \tag{A.15}$$

Thus, by rearranging Eq. (A.14) we arrive at the Cramér-Rao bound:

$$\mathrm{Var}[\hat{g}] \geq \frac{1}{F(g)}. \tag{A.16}$$

This same reasoning can be used in the case of N independent measurements, which will only change $F(g)$ to $NF(g)$ in Eq. (A.16).

Bibliography

[1] B. P. Abbott et al. “Observation of Gravitational Waves from a Binary Black Hole Merger”. In: *Phys. Rev. Lett.* 116 (6 Feb. 2016), p. 061102. DOI: 10.1103/PhysRevLett.116.061102. URL: https://link.aps.org/doi/10.1103/PhysRevLett.116.061102.

[2] Yakir Aharonov, David Z. Albert, and Lev Vaidman. “How the result of a measurement of a component of the spin of a spin-1/2 particle can turn out to be 100”. In: *Phys. Rev. Lett.* 60 (14 Apr. 1988), pp. 1351–1354. DOI: 10.1103/PhysRevLett.60.1351. URL: https://link.aps.org/doi/10.1103/PhysRevLett.60.1351.

[3] Yakir Aharonov et al. “Quantum Cheshire Cats”. In: *New Journal of Physics* 15.11 (Nov. 2013), p. 113015. DOI: 10.1088/1367-2630/15/11/113015. URL: https://doi.org/10.1088/1367-2630/15/11/113015.

[4] Domenico Alj et al. “Polar POLICRYPS diffractive structures generate cylindrical vector beams”. In: *Applied Physics Letters* 107 (Nov. 2015), p. 201101. DOI: 10.1063/1.4935605.

[5] L. Allen et al. “Orbital angular momentum of light and the transformation of Laguerre-Gaussian laser modes”. In: *Phys. Rev. A* 45 (11 June 1992), pp. 8185–8189. DOI: 10.1103/PhysRevA.45.8185. URL: https://link.aps.org/doi/10.1103/PhysRevA.45.8185.

[6] Alain Aspect. “Bell’s inequality test: more ideal than ever”. In: *Nature* 398.6724 (Mar. 1999), pp. 189–190. ISSN: 1476-4687. DOI: 10.1038/18296. URL: https://doi.org/10.1038/18296.

[7] W. F. Balthazar et al. “Tripartite nonseparability in classical optics”. In: *Opt. Lett.* 41.24 (Dec. 2016), pp. 5797–5800. DOI: 10.1364/OL.41.005797. URL: http://opg.optica.org/ol/abstract.cfm?URI=ol-41-24-5797.

[8] GianPiero Banfi, Vittorio Degiorgio, and Burkhard Speit. “Neutron scattering investigation of the structure of semiconductor-doped glasses”. In: *Journal of Applied Physics* 74.11 (1993), pp. 6925–6935. DOI: 10.1063/1.355067. eprint: https://doi.org/10.1063/1.355067. URL: https://doi.org/10.1063/1.355067.

[9] J. S. Bell. “On the Einstein Podolsky Rosen paradox”. In: *Physics Physique Fizika* 1 (3 Nov. 1964), pp. 195–200. DOI: 10.1103/PhysicsPhysiqueFizika.1.195. URL: https://link.aps.org/doi/10.1103/PhysicsPhysiqueFizika.1.195.

[10] Charles H. Bennett et al. “Teleporting an unknown quantum state via dual classical and Einstein-Podolsky-Rosen channels”. In: *Phys. Rev. Lett.* 70 (13 Mar. 1993), pp. 1895–1899. DOI: 10.1103/PhysRevLett.70.1895. URL: https://link.aps.org/doi/10.1103/PhysRevLett.70.1895.

[11] K.S. Bindra, S.M. Oak, and K.C. Rustagi. “Optical limiting in semiconductor-doped glasses”. In: *Optics Communications* 124.5 (1996), pp. 452–456. ISSN: 0030-4018. DOI: https://doi.org/10.1016/0030-4018(95)00716-4. URL: https://www.sciencedirect.com/science/article/pii/0030401895007164.

[12] Matthias Bock et al. “Highly efficient heralded single-photon source for telecom wavelengths based on a PPLN waveguide”. In: *Opt. Express* 24.21 (Oct. 2016), pp. 23992–24001. DOI: 10.1364/OE.24.023992. URL: http://www.osapublishing.org/oe/abstract.cfm?URI=oe-24-21-23992.

[13] David Bohm. *Quantum Theory*. 1st edition. Prentice Hall, 1951.

[14] C. V. S. Borges et al. “Bell-like inequality for the spin-orbit separability of a laser beam”. In: *Phys. Rev. A* 82 (3 Sept. 2010), p. 033833. DOI: 10.1103/PhysRevA.82.033833. URL: https://link.aps.org/doi/10.1103/PhysRevA.82.033833.

[15] D. Boschi et al. “Experimental Realization of Teleporting an Unknown Pure Quantum State via Dual Classical and Einstein-Podolsky-Rosen Channels”. In: *Phys. Rev. Lett.* 80 (6 Feb. 1998), pp. 1121–1125. DOI: 10.1103/PhysRevLett.80.1121. URL: https://link.aps.org/doi/10.1103/PhysRevLett.80.1121.

[16] Robert W. Boyd. *Nonlinear Optics*. Third edition. Academic Press, 2008.

[17] Nicolas Brunner and Christoph Simon. “Measuring Small Longitudinal Phase Shifts: Weak Measurements or Standard Interferometry?” In: *Phys. Rev. Lett.* 105 (1 July 2010), p. 010405. DOI: 10.1103/PhysRevLett.105.010405. URL: https://link.aps.org/doi/10.1103/PhysRevLett.105.010405.

[18] Demetrios N. Christodoulides et al. “Nonlinear refraction and absorption: mechanisms and magnitudes”. In: *Adv. Opt. Photon.* 2.1 (Mar. 2010), pp. 60–200. DOI: 10.1364/AOP.2.000060. URL: http://opg.optica.org/aop/abstract.cfm?URI=aop-2-1-60.

[19] John F. Clauser et al. “Proposed Experiment to Test Local Hidden-Variable Theories”. In: *Phys. Rev. Lett.* 23 (15 Oct. 1969), pp. 880–884. DOI: 10.1103/PhysRevLett.23.880. URL: https://link.aps.org/doi/10.1103/PhysRevLett.23.880.

[20] Claude Cohen-Tannoudji, Bernard Diu, and Frank Laloë. *Quantum Mechanics*. 2nd edition. Vol. 1. Wiley, 1977.

[21] Raul Corrêa et al. “‘Quantum Cheshire Cat’ as simple quantum interference”. In: *New Journal of Physics* 17.5 (May 2015), p. 053042. DOI: 10.1088/1367-2630/17/5/053042. URL: https://doi.org/10.1088/1367-2630/17/5/053042.

[22] H. Cramér. *Mathematical Methods of Statistics*. First edition. Princeton University Press, 1946.

[23] P. Ben Dixon et al. “Ultrasensitive Beam Deflection Measurement via Interferometric Weak Value Amplification”. In: *Phys. Rev. Lett.* 102 (17 Apr. 2009), p. 173601. DOI: 10.1103/PhysRevLett.102.173601. URL: https://link.aps.org/doi/10.1103/PhysRevLett.102.173601.

[24] Justin Dressel et al. “Colloquium: Understanding quantum weak values: Basics and applications”. In: *Rev. Mod. Phys.* 86 (1 Mar. 2014), pp. 307–316. DOI: 10.1103/RevModPhys.86.307. URL: https://link.aps.org/doi/10.1103/RevModPhys.86.307.

[25] Patrick Egan and Jack A. Stone. "Weak-value thermostat with 0.2 mK precision". In: *Opt. Lett.* 37.23 (Dec. 2012), pp. 4991–4993. DOI: 10.1364/OL.37.004991. URL: http://opg.optica.org/ol/abstract.cfm?URI=ol-37-23-4991.

[26] A. Einstein, B. Podolsky, and N. Rosen. "Can Quantum-Mechanical Description of Physical Reality Be Considered Complete?" In: *Phys. Rev.* 47 (10 May 1935), pp. 777–780. DOI: 10.1103/PhysRev.47.777. URL: https://link.aps.org/doi/10.1103/PhysRev.47.777.

[27] Manuel R. Ferdinandus et al. "Beam deflection measurement of time and polarization resolved ultrafast nonlinear refraction". In: *Opt. Lett.* 38.18 (Sept. 2013), pp. 3518–3521. DOI: 10.1364/OL.38.003518. URL: http://opg.optica.org/ol/abstract.cfm?URI=ol-38-18-3518.

[28] Vinícius Castro Ferreira. "Espectroscopia ótica não linear em anel antirressonante". PhD thesis. Universidade Federal do Rio Grande do Sul, 2020. URL: http://hdl.handle.net/10183/217483.

[29] Partha Ghose and Anirban Mukherjee. *Entanglement in Classical Optics*. 2013. arXiv: 1308.6154 [physics.optics].

[30] Joseph W. Goodman. *Introduction to Fourier Optics*. 3rd edition. Roberts & Company, 2004.

[31] David J. Griffiths. *Introduction to Electrodynamics*. 4th edition. Cambridge University Press, 2017.

[32] David J. Griffiths. *Introduction to Quantum Mechanics*. 1st edition. Prentice Hall, 1995.

[33] Seyed Mohammad Hashemi Rafsanjani et al. "State transfer based on classical nonseparability". In: *Phys. Rev. A* 92 (2 Aug. 2015), p. 023827. DOI: 10.1103/PhysRevA.92.023827. URL: https://link.aps.org/doi/10.1103/PhysRevA.92.023827.

[34] Alex Hayat, Amir Steinberg, and Aephraim Steinberg. "Enhancing metrology sensitivity by weak measurements". In: *SPIE Newsroom* (Dec. 2011), pp. 1–2.

[35] Eugene Hecht. *Optics*. 5th edition. Pearson, 2017.

[36] J. M. Hogan et al. "Precision angle sensor using an optical lever inside a Sagnac interferometer". In: *Opt. Lett.* 36.9 (May 2011), pp. 1698–1700. DOI: 10.1364/OL.36.001698. URL: http://opg.optica.org/ol/abstract.cfm?URI=ol-36-9-1698.

[37] Ryszard Horodecki et al. "Quantum entanglement". In: *Rev. Mod. Phys.* 81 (2 June 2009), pp. 865–942. DOI: 10.1103/RevModPhys.81.865. URL: https://link.aps.org/doi/10.1103/RevModPhys.81.865.

[38] Onur Hosten and Paul Kwiat. "Observation of the Spin Hall Effect of Light via Weak Measurements". In: *Science* 319.5864 (2008), pp. 787–790. DOI: 10.1126/science.1152697. eprint: https://www.science.org/doi/pdf/10.1126/science.1152697. URL: https://www.science.org/doi/abs/10.1126/science.1152697.

[39] John C. Howell et al. "Interferometric weak value deflections: Quantum and classical treatments". In: *Phys. Rev. A* 81 (3 Mar. 2010), p. 033813. DOI: 10.1103/PhysRevA.81.033813. URL: https://link.aps.org/doi/10.1103/PhysRevA.81.033813.

[40] Meng-Jun Hu, Shuai Zha, and Yong-Sheng Zhang. *Quantum Enhanced Interferometer for Kilohertz Gravitational Wave Detection*. 2021. arXiv: 2007.03978 [astro-ph.IM].

[41] Jing-Hui Huang, Xue-Ying Duan, and Xiang-Yun Hu. “Amplification of rotation velocity using weak measurements in Sagnac’s interferometer”. In: *The European Physical Journal D* 75.3 (Mar. 2021). ISSN: 1434-6079. DOI: 10.1140/epjd/s10053-021-00117-4. URL: http://dx.doi.org/10.1140/epjd/s10053-021-00117-4.

[42] John D. Jackson. *Classical Electrodynamics*. 2nd edition. John Wiley & Sons, 1975.

[43] W. B. Jackson et al. “Photothermal deflection spectroscopy and detection”. In: *Appl. Opt.* 20.8 (Apr. 1981), pp. 1333–1344. DOI: 10.1364/AO.20.001333. URL: http://opg.optica.org/ao/abstract.cfm?URI=ao-20-8-1333.

[44] Kumel H. Kagalwala et al. “Bell’s measure in classical optical coherence”. In: *Nature Photonics* 7.1 (Jan. 2013), pp. 72–78. ISSN: 1749-4893. DOI: 10.1038/nphoton.2012.312. URL: https://doi.org/10.1038/nphoton.2012.312.

[45] Lea Kopf et al. “Spectral vector beams for high-speed spectroscopic measurements”. In: *Optica* 8.6 (June 2021), pp. 930–935. DOI: 10.1364/OPTICA.424960. URL: http://opg.optica.org/optica/abstract.cfm?URI=optica-8-6-930.

[46] Parveen Kumar, Kyrylo Snizhko, and Yuval Gefen. “Engineering two-qubit mixed states with weak measurements”. In: *Physical Review Research* 2.4 (Oct. 2020). ISSN: 2643-1564. DOI: 10.1103/physrevresearch.2.042014. URL: http://dx.doi.org/10.1103/PhysRevResearch.2.042014.

[47] Serge Lang. *Linear Algebra*. 3rd edition. Springer, 2004.

[48] Wei-Tao Liu et al. “Anomalous amplification of a homodyne signal via almost-balanced weak values”. In: *Opt. Lett.* 42.5 (Mar. 2017), pp. 903–906. DOI: 10.1364/OL.42.000903. URL: http://opg.optica.org/ol/abstract.cfm?URI=ol-42-5-903.

[49] Rodney Loudon. *The quantum theory of light*. 3rd edition. Oxford University Press, 2000.

[50] Kevin Lyons, John C. Howell, and Andrew N. Jordan. “Noise suppression in inverse weak value-based phase detection”. In: *Quantum Studies: Mathematics and Foundations* 5.4 (Oct. 2017), pp. 579–588. ISSN: 2196-5617. DOI: 10.1007/s40509-017-0145-7. URL: http://dx.doi.org/10.1007/s40509-017-0145-7.

[51] Xiao-Song Ma et al. “Quantum teleportation over 143 kilometres using active feed-forward”. In: *Nature* 489.7415 (Sept. 2012), pp. 269–273. ISSN: 1476-4687. DOI: 10.1038/nature11472. URL: https://doi.org/10.1038/nature11472.

[52] Omar S. Magaña-Loaiza et al. “Amplification of Angular Rotations Using Weak Measurements”. In: *Phys. Rev. Lett.* 112 (20 May 2014), p. 200401. DOI: 10.1103/PhysRevLett.112.200401. URL: https://link.aps.org/doi/10.1103/PhysRevLett.112.200401.

[53] Julían Rodrigo Martínez-Ríncon. “Weak-Values Metrological Techniques for Parameter Estimation”. PhD thesis. University of Rochester, 2017.

[54] Julián Martínez-Rincón et al. “Can Anomalous Amplification be Attained without Postselection?” In: *Phys. Rev. Lett.* 116 (10 Mar. 2016), p. 100803. DOI: 10.1103/PhysRevLett.116.100803. URL: https://link.aps.org/doi/10.1103/PhysRevLett.116.100803.

[55] John von Neumann. *Mathematische Gründlagen der Quantemechanik*. 1st edition. (English translation: *Mathematical Foundations of Quantum Mechanics*, Princeton University Press, 1955). Springer-Verlag, 1932.

[56] *Optical Filter Glass (Data Sheets)*. Schott AG. Aug. 2021.

[57] L. J. Pereira, A. Z. Khoury, and K. Dechoum. "Quantum and classical separability of spin-orbit laser modes". In: *Phys. Rev. A* 90 (5 Nov. 2014), p. 053842. DOI: 10.1103/PhysRevA.90.053842. URL: https://link.aps.org/doi/10.1103/PhysRevA.90.053842.

[58] Xiao-Feng Qian, A. Nick Vamivakas, and Joseph H. Eberly. "Emerging Connections: Classical and Quantum Optics". In: *Opt. Photon. News* 28.10 (Oct. 2017), pp. 34–41. DOI: 10.1364/OPN.28.10.000034. URL: http://www.optica-opn.org/abstract.cfm?URI=opn-28-10-34.

[59] Mushegh Rafayelyan. "Singular beam shaping from spin-orbit flat optics". PhD thesis. May 2017. DOI: 10.13140/RG.2.2.23241.34403.

[60] P. Réfrégier. *Noise Theory and Application to Physics*. First edition. Springer New York, 2004.

[61] Matthew Reichert et al. "Beam deflection measurement of bound-electronic and rotational nonlinear refraction in molecular gases". In: *Opt. Express* 23.17 (Aug. 2015), pp. 22224–22237. DOI: 10.1364/OE.23.022224. URL: http://opg.optica.org/oe/abstract.cfm?URI=oe-23-17-22224.

[62] M. D. Reid et al. "Colloquium: The Einstein-Podolsky-Rosen paradox: From concepts to applications". In: *Rev. Mod. Phys.* 81 (4 Dec. 2009), pp. 1727–1751. DOI: 10.1103/RevModPhys.81.1727. URL: https://link.aps.org/doi/10.1103/RevModPhys.81.1727.

[63] J. J. Sakurai. *Modern Quantum Mechanics*. Revised ed. Addison-Wesley, 1994.

[64] B. N. Simon et al. "Nonquantum Entanglement Resolves a Basic Issue in Polarization Optics". In: *Phys. Rev. Lett.* 104 (2 Jan. 2010), p. 023901. DOI: 10.1103/PhysRevLett.104.023901. URL: https://link.aps.org/doi/10.1103/PhysRevLett.104.023901.

[65] Jonathan D. Spear and Richard E. Russo. "Transverse photothermal beam deflection within a solid". In: *Journal of Applied Physics* 70.2 (1991), pp. 580–586. DOI: 10.1063/1.349659. URL: https://doi.org/10.1063/1.349659.

[66] David J. Starling et al. "Optimizing the signal-to-noise ratio of a beam-deflection measurement with interferometric weak values". In: *Phys. Rev. A* 80 (4 Oct. 2009), p. 041803. DOI: 10.1103/PhysRevA.80.041803. URL: https://link.aps.org/doi/10.1103/PhysRevA.80.041803.

[67] David J. Starling et al. "Precision frequency measurements with interferometric weak values". In: *Phys. Rev. A* 82 (6 Dec. 2010), p. 063822. DOI: 10.1103/PhysRevA.82.063822. URL: https://link.aps.org/doi/10.1103/PhysRevA.82.063822.

[68] Grégory Strübi and C. Bruder. "Measuring Ultrasmall Time Delays of Light by Joint Weak Measurements". In: *Phys. Rev. Lett.* 110 (8 Feb. 2013), p. 083605. DOI: 10.1103/PhysRevLett.110.083605. URL: https://link.aps.org/doi/10.1103/PhysRevLett.110.083605.

[69] Bengt Svensson. "Pedagogical Review of Quantum Measurement Theory with an Emphasis on Weak Measurements". In: *Quanta* 2.1 (2013), pp. 18–49. ISSN: 1314-7374. DOI: 10.12743/quanta.v2i1.12. URL: http://quanta.ws/ojs/index.php/quanta/article/view/12.

[70] Gerardo I. Viza et al. “Complementary weak-value amplification with concatenated postselections”. In: *Phys. Rev. A* 94 (4 Oct. 2016), p. 043825. DOI: `10.1103/PhysRevA.94.043825`. URL: `https://link.aps.org/doi/10.1103/PhysRevA.94.043825`.

[71] Amnon Yariv. *Quantum Electronics*. 3rd edition. John Wiley & Sons, 1988.

[72] Peng Zhao et al. “Temporal and polarization dependence of the nonlinear optical response of solvents”. In: *Optica* 5.5 (May 2018), pp. 583–594. DOI: `10.1364/OPTICA.5.000583`. URL: `http://opg.optica.org/optica/abstract.cfm?URI=optica-5-5-583`.

[73] Xinxing Zhou et al. “Experimental observation of the spin Hall effect of light on a nanometal film via weak measurements”. In: *Phys. Rev. A* 85 (4 Apr. 2012), p. 043809. DOI: `10.1103/PhysRevA.85.043809`. URL: `https://link.aps.org/doi/10.1103/PhysRevA.85.043809`.